VALIDATION OF DIFFUSION TENSOR IMAGING MEASURES OF

CORTICOCORTICAL CONNECTIVITY IN THE BRAIN

By

Yurui Gao

Dissertation

Submitted to the Faculty of the

Graduate School of Vanderbilt University

in partial fulfillment of the requirements

for the degree of

DOCTOR OF PHILOSOPHY

in

Biomedical Engineering

May, 2013

Nashville, Tennessee

Approved:

Professor Adam W. Anderson

Professor Malcolm J. Avison

Professor Mark D. Does

Professor Iwona Stepniewska

Professor Zhaohua Ding

To my father, Qunlin Gao, and mother, Xiangrong Li,

for their support and love

and

To my baby boy, Julian Chen, for bringing me lifelong joy

ACKNOWLEDGEMENTS

ABSTRACT

Diffusion tensor imaging (DTI) provides a unique approach to probing the microstructure of biological tissues noninvasively and DTI-based tractography is an irreplaceable tool to measure anatomical connectivity in human brain *in vivo*. However, due to the limitations of DTI techniques and tractography algorithms, tracked pathways might not be completely accurate. Thus, quantifying the agreement between DTI tractography and histological measurements of true fiber pathways is critical for progress in the field. A series of validation studies of DTI tractography is presented in this thesis, including (1) assessment of the relationship between DTI tractography-derived corticocortical connectivity and histological 'ground truth' on a regional and voxelwise basis; (2) localizing the divergence between DTI tractography and histology, followed by qualitative analysis of the reasons for those discrepancies. The work presented here is based on a non-human primate animal model, which has comparable parameters to magnetic resonance imaging (MRI) human data, and thus provides an important guide to interpreting the results of DTI-based tractography measures in the human brain.

TABLE OF CONTENTS

LIST OF TABLES

LIST OF FIGURES

LIST OF ABBREVIATIONS

2D/3D	Two/Three dimensional
ARD	Automatic relevance determination
A	Anterior
BDA	Biotinylated dextran amine
CC	Correlation coefficient
DDM	Density distribution map
DSI	Diffusion spectrum imaging
DTI	Diffusion tensor imaging
DWI	Diffusion weighted imaging
FA	Fractional anisotropy
fMRI	Functional magnetic resonance imaging
FOD	Fiber orientation distribution
FOV	Field of view
HARDI	High angular resolution diffusion imaging
hFOD	Histological fiber orientation distribution

I	Inferior
IR	Injection region
iAC/cAC	ipsilateral/contralateral anterior cingulate cortex
iM1/cM1	ipsilateral/contralateral primary motor cortex
iPA/cPA	ipsilateral/contralateral anterior parietal cortex
iPP/cPP	ipsilateral/contralateral posterior parietal cortex
iPF/cPF	ipsilateral/contralateral prefrontal cortex
iPM/cPM	ipsilateral/contralateral premotor cortex
iPVR/cPVR	ipsilateral/contralateral parietal ventral and rostral areas of lateral sulcus
iS2/cS2	ipsilateral/contralateral secondary somatosensory cortex
iSMA/cSMA	ipsilateral/contralateral supplementary motor area
L	Left
M1	Primary motor cortex
MRI	Magnetic resonance imaging
P	Posterior
PGSE	Pulsed gradient spin echo

PPD   Preservation of principal direction

R   Right

RF   Radio frequency

ROI   Region of interest

S   Superior

SNR   Signal to noise ratio

TE   Echo time

TR   Repetition time

WGM   White-Grey matter

LIST OF SYMBOLS

δ	Diffusion gradient duration
Δ	Diffusion time
D	Diffusion coefficient
$\boldsymbol{D}$	Diffusion tensor
$\vec{e}$	Eigenvector
G	Gradient strength
λ	Eigenvalue

CHAPTER I

INTRODUCTION

1.1 Objective and Specific Aims

Diffusion tensor imaging (DTI) is a technique for non-invasive measurement of the structural connectivity of the brain. Like any other measuring technique, DTI has limitations in accuracy and precision. Therefore, it is necessary to validate the DTI technique as a measure of structural connectivity. The long term objective of this study is to investigate the relationship (i.e., agreement and discrepancy) between structural connectivity measured by DTI tractography and the 'ground truth' connectivity measured by anatomical procedures in an animal model. Two specific aims for this study are as follows:

1. Quantify the correspondence between DTI tractography and histology derived connectivity.

   a. We quantify the correspondence of connectivity strength derived from DTI tractography (using both deterministic and probabilistic algorithms) and from an anatomical tracer across all cortical regions that have well-known connections to the primary motor cortex. We test the following hypotheses: 1) the number of DTI derived streamlines is proportional to the histological connectivity strength across functional regions; 2) DTI tractography is better able to reveal true inter-regional connectivity for those cortical regions with

stronger connections to the primary motor cortex. Measurements of weaker connections are less reliable.

b. We quantitatively compare the DTI-tractography-derived streamline distribution (using both deterministic and probabilistic algorithms) on the white/grey matter interface with the histological fiber distribution within each specific cortical region that has well-known connections with the primary motor cortex. We test two hypotheses: 1) the number of DTI derived streamlines is proportional to the histological connectivity strength within a functional region; 2) DTI tractography is more likely to reveal the true fiber distribution within cortical regions with stronger connections to primary motor cortex.

2. Localize and analyze the divergence between DTI tractography and histology derived connectivity.

We first localize the voxels where DTI streamlines deviated from histological pathways (so called 'error' voxels) by superimposing 3D histological fiber pathways on the DTI-tractography-derived streamlines. Then we quantitatively analyze the underlying reasons (e.g., crossing fibers) for some 'error' voxel. We test the hypothesis that DTI tractography reconstructs the true fiber pathways in regions of parallel fibers with less fitting error, but is more likely to make errors in regions of crossing fibers.

1.2 Significance

DTI tractography has become the one of most popular tools to investigate structural connections in the human brain because this technique obviates the invasiveness of traditional methods, the so called 'gold standard' of neuroanatomy. However, it is not clear to what extent DTI tractography can reveal true anatomical connectivity. A number of well-examined factors (e.g., signal to noise ratio, partial volume effects, imperfect tensor model and tractography algorithms) challenge the fidelity with which DTI tractography can accurately reveal anatomical structures, hence the agreement between tractography-derived and anatomical connectivity needs to be evaluated quantitatively. Moreover, further analysis of the possible reasons for disagreements between these two connectivity measures could help to understand better the limitations of DTI tractography. This, in turn, would help to improve interpretation of tractography results and optimize the employment of this technique in further studies of human brain connectivity.

CHAPTER II

BACKGROUND

2.1 Diffusion Tensor Imaging

Diffusion tensor imaging (DTI) is capable of noninvasively probing the microstructure of biological tissue [1]. It has been applied in a wide variety of studies on human brain in health and disease, including stroke [2], multiple sclerosis [3, 4], Alzheimer's disease [5, 6], depression [7], schizophrenia [8] , autism [9] and normal brain development [10, 11].

"Diffusion" in the term Diffusion Tensor Imaging refers to Brownian motion of water molecules. Assuming free diffusion, Einstein proved that the mean squared displacements of water molecules, $\langle r^2 \rangle$, is directly proportional to the diffusion time, t, and self-diffusion coefficient, D, [12], given by

$$\langle r^2 \rangle = nDt, \tag{2.1-1}$$

where n is a numerical constant that depends on dimensionality ($n = 2$, 4, or 6, for 1, 2, or 3 dimensional diffusion). This random thermal motion of spins reduces the amplitude of the spin echo signal in the presence of a magnetic field inhomogeneity, an effect first observed by Hahn [13] and theoretically described by Carr, Purcell [14] and Bloch-Torrey [15].

In diffusion imaging, it is the diffusion coefficient, D, that is inferred from measurements of mean squared water displacement over a given diffusion time. If the

4

diffusing water molecules encounter any hindrances or restrictions along their random walk, the calculated diffusion coefficient (the so-called apparent diffusion coefficient, ADC) will be lower than the free diffusion coefficient.

Stejskal and Tanner [16] developed the pulsed gradient spin-echo (PGSE) [16] sequence to measure the molecular diffusion coefficients directly and quantitatively. This pulse sequence is shown in Figure 2.1-1: the diffusion-encoding gradient is applied in two matched pulses (blue squares) with equal magnitude G and duration δ, placed on each side of the 180˚ RF pulse, with leading edges separated by an interval Δ.
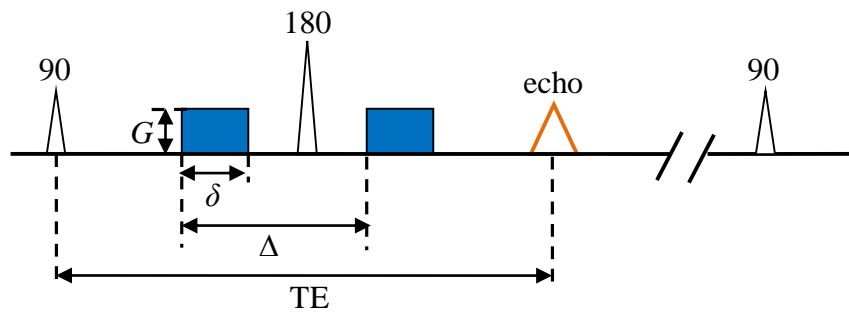
Figure 2.1-1. Timing diagram of a PGSE sequence. The bipolar diffusion pulses (blue squares) with magnitude G and duration δ, are placed on each side of the 180˚ refocusing pulse, with leading edges separated by an interval Δ. All other gradients required for imaging are ignored in this diagram.

Employing the PGSE sequence with diffusion gradient applied along a single direction, the diffusion weighted (DW) signal, S_1, is attenuated relative to the non-DW signal, S_0, by a factor given by the exponential product of the diffusion weighting '*b value*' and the ADC along that diffusion gradient direction, where *b* is given by

$$b = \gamma^2 G^2 \delta^2 \left(\Delta - \frac{\delta}{3} \right), \tag{2.1-2}$$

and γ is the gyromagnetic ratio. To characterize anisotropic diffusion in biological tissue, Basser *et al.* [1, 17] introduced a diffusion tensor model, defined by

$$\boldsymbol{D} = \begin{vmatrix} D_{xx} & D_{xy} & D_{xz} \\ D_{xy} & D_{yy} & D_{yz} \\ D_{xz} & D_{yz} & D_{zz} \end{vmatrix}, \tag{2.1-3}$$

where *Dxx*, *Dyy* and *Dzz* correspond to diffusivities along three orthogonal axes, while *Dxy*, *Dxz* and *Dyz* correspond to the correlations between the displacements along the orthogonal axes. Given the tensor model, we have:

$$S_i = S_0 e^{-b g_i^T \boldsymbol{D} g_i}, \text{ with } i = 1,2,\dots,N, \tag{2.1-4}$$

where $\boldsymbol{g_i}$ is a unit vector representing the direction of the ith diffusion gradient, S_i is the DW signal for that direction and N is the total number of diffusion gradients. Diagonalizing $\boldsymbol{D}$ yields three eigenvectors ($\boldsymbol{v_1}$, $\boldsymbol{v_2}$, $\boldsymbol{v_3}$) and their corresponding eigenvalues (λ_1, λ_2, λ_3; $\lambda_1 \geq \lambda_2 \geq \lambda_3$). The eigenvectors identify the symmetry axes of diffusion while the eigenvalues are the diffusion coefficients along the axes. Since water diffusion is anisotropically hindered by structural elements in organized tissue, especially by ordered fibers [18], the diffusion tensor serves as a sensitive probe of fiber orientation [19].

2.2 Tractography

Diffusion imaging lays a foundation to reconstruct neural fiber pathways by tracking

fiber orientations inferred from the diffusion tensor. The reconstruction of fiber pathways based on diffusion imaging data is referred to as DTI tractography. Among the many tractography methods that have been developed [20-25], the deterministic streamline method, based on a single tensor model, and a Bayesian method with a multi-tensor model [26] are our focus because of their wide adoption in human brain research and implementation in mature software, such as DTIStudio (DS, http://mristudio.org/) and the FMRIB (Functional Magnetic Resonance Imaging of the Brain, Oxford, UK) software library (FSL, http://fmrib.ox.ac.uk/fsl/).

The most intuitive way of reconstructing a 3D streamline from a field of single-tensors is to propagate a line (so called 'streamline') from a seed point by following the primary eigenvector direction of the tensor as the local fiber orientation. The key point to achieve a smooth streamline is to propagate with a small step size (smaller than 1/3 pixel width or height) and move along the distance-averaged orientation within the local neighborhood, as shown in Figure 2.2-1. Such streamline propagation is terminated when the anisotropy falls below a threshold value or the propagation direction changes by too large an angle (the 'bending' angle) between steps. These stopping criteria are based on underlying assumptions that low anisotropy tends to be associated with high uncertainty in the primary diffusion direction and that a sharp turn between consecutive steps is more likely to be caused by erroneous measurement than fiber biophysics. The advantages of this simple approach to streamline tractography are conceptual straightforwardness and computational efficiency.
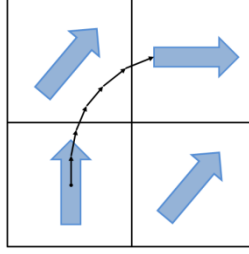
Figure 2.2-1. Schematic plot of the interpolation approach to performing tract propagation. The large blue arrows indicate the fiber orientations estimated from diffusion tensors. Each small black arrow shows the distance-weighted average of nearby orientations for one propagating step [27].

Considering the uncertainty of fiber orientation estimation, Behrens *et al.* proposed a probabilistic method based on a multiple fiber model [25]. They used Bayesian estimation to fit the parameters of the multi-compartment model as follows:

$$S_i = S_0 \left(\left(1 - \sum_{j=1}^{N} f_j\right) e^{-bd} + \sum_{j=1}^{N} f_j \, e^{-bd g_i^T R_j A R_j^T g_i} \right) \quad \left(A = \begin{pmatrix} 1 & 0 & 0 \\ 0 & 0 & 0 \\ 0 & 0 & 0 \end{pmatrix}\right), \quad (2.2\text{-}1)$$

where d is the diffusivity, f_j and $R_j A R_j^T$ are the signal fraction and orientation of the jth fiber, and N is the maximum number of fibers. Instead of progressing along the most likely primary diffusion direction, sample streamlines are draw from posterior distributions on a set of diffusion directions, and each orientation, i, is chosen with a probability proportional to f_j at each step. In a crossing fiber region, the tracking scheme will tend to maintain the previous orientation of the streamline, allowing the tracking of non-dominant pathways through the crossing regions.

Compared to the deterministic streamline method, the Bayesian approach is better

able to handle partial volume effects, but is also much slower due to the large amount of sampling required. Therefore, both tractography approaches have become common research tools for *in vivo* studies of neural tissue morphology, pathway location, and other properties which directly relate to the neuropsychiatric/neurologic disorders [8], brain organization and development [10, 11].

2.3 Measurement of Brain Structural Connectivity

Structural connectivity of the human brain is the anatomical basis of brain function. Knowledge of structural connectivity is fundamental to understanding the organization of the brain and its response to disease and injury. The two major categories of connectivity measurements–anatomical measurement and DTI tractography-based measurement--are briefly described next.

2.3.1 Anatomical measurement

Early experimental methods to reveal connectivity employed gross dissection [28] and bare neural degeneration procedures [29-31], which provided limited visibility for observing neural pathways and severe damage to the brain tissue. Contemporary experimental tracking relies on exploiting various neural tracers, which capitalize on cytoplasmic flow mediated specifically by the axoplasmic transport system [32], starting from horseradish peroxidase (HRP) [33, 34], lectins [35], toxins [36] and their conjugates [37], followed by fluorescent compounds [38, 39], dextrans and viruses [40]. Tracer methods provide much more connectivity detail, yet the whole acquisition process is

labor intensive and again, their highly invasive nature prevents their implementation for *in vivo* connectivity mapping.

2.3.2 DTI tractography-based measurement

DTI tractography overcomes the problem of invasiveness in brain mapping. In 1999, **Xue** *et al*. reconstructed eight well-known fiber bundles in the anesthetized rat brain using the Fiber Assignment by Continuous Tracking (FACT) algorithm [21], which was the first example of *in vivo* tractography using an animal model [41]. **Catani** *et al*. applied a streamline procedure to visualize major white matter fasciculi (e.g., the superior longitudinal fasciculus and inferior longitudinal fasciculus) within the living human brain [42]. However, those deterministic tractography-derived connectivity probes were assumed to provide limited accuracy and angular resolution in complex fiber structures (e.g., crossing, kissing, bending and merging fibers) within a voxel. To include the effect of uncertainty of fiber orientation estimation, probabilistic tractography strategies appeared and bloomed, and were applied to exploratory studies of connectivity. The **Hagmann** group first employed a statistical random-walk algorithm to reconstruct white matter density maps, which offered a measure of the probability that a given voxel connects with the white matter region of interest (ROI) [43]. Further progress was made on corticocortical mapping using DTI tractography approaches. **Behrens** *et al.* first qualitatively identified anatomical connections between human grey matter structures (i.e., thalamus and cortex) using a probabilistic tractography algorithm and moreover subdivided the human thalamus based on connectivity to predefined cortical targets [44]. **Johansen-berg** *et al*. performed a similar tractography analysis to derive connectivity

profiles for points along cortical ROIs and then used the changes in connectivity profiles to define functionally distinct regions, i.e., the supplementary motor area (SMA) and pre-SMA [45]. A common assumption used in most connectivity research is that a greater number of calculated fibers or samples within one voxel (also termed higher density) indicates higher connectivity between the seed region and this voxel.

2.4 Validation Studies

Despite the promise of MRI-based connectivity measurements, a concern about the accuracy of DTI tractography is inevitable: to what extent does it reflect 'ground truth' anatomical connectivity? A number of well-known factors (e.g., signal to noise ratio [46] and partial volume effect [47]) may limit the reliability of DTI tractography [48]. For this reason, the agreement between tractography-derived and true anatomical connectivity needs to be fully evaluated. Existing *in vivo* or *in vitro* validation studies [49-51] mainly involve comparing tractography-derived pathways with the 'ground truth' white matter fiber tracts obtained by means of surgical dissection, histological tracer tracking and MR-visible tracer tracking in different species, which will be discussed below.

From averaged DTI data of 15 human subjects, **Lawes** *et al*. constructed a white matter atlas by assigning each individual streamline to a predefined-cortical-connected tract based on the location of the termination of this streamline and then qualitatively compared those tracts with corresponding dissected fasciculi. The observational result showed a close correspondence between tracts generated from the atlas and grossly dissected tracts [49].

Surgical dissection based validation could only assess tract correspondence on a relatively coarse scale. Histochemical procedures, conversely, allow more detail to be visualized. **Burgel** *et al.* used modified myelin stained histological sections of ten postmortem human brains to reconstruct 3D registered maps of the topography, course and intersubject variability of major fiber tracts in an MRI reference space [52]. Their purpose in making these microstructural maps was to evaluate DTI fiber bundles qualitatively, although they didn't perform any direct comparison in this study.

As an alternative to non-selectively staining the myelinated fibers throughout a section of the brain, a number of neural tracers can be transported inside axons and thus used to investigate the connectivity of specific tracts. **Dauguet** *et al.* injected wheat germ agglutinin conjugated to horseradish peroxidase (WGA-HRP) into a cortical region of a macaque monkey and compared the WGA-HRP labeled white matter region with DTI streamlines in the MRI space [51]. *In vivo* diffusion weighted imaging (DWI) was performed on the same monkey and tractography was implemented using a standard hyperstreamline-based method [23] with the transformed WGA-HRP injection region as the seed region. The spatial similarity between histology and DTI tractography was defined by the Dice coefficient [53] and found to be high in their experiment.

The paramagnetic manganese ion (Mn^{2+}), a MR-visible tracer, can highlight many pathways because it shortens T1 and is transported in axons. Its use as a 'gold standard' is not established, as the specificity of the tracer needs further investigation [48], but a number of validation experiments on the basis of manganese tracing have been performed. **Dyrby** *et al.*, validated probabilistic tractography against both histological and MR-

visible tracers in three porcine brains [50]. Biotinylated dextran amine (BDA) and manganese chloride ($MnCl_2$) were injected into the right somatosensory cortex (SC), the right prefrontal cortex (PFC), or left motor cortex (MC) separately in the three brains. The DWI images were acquired both *in vivo* and *in vitro* and the Probabilistic Index of Connectivity (PICo) algorithm [54] was used to track the fibers originating from injection sites. To measure the spatial agreement between white matter regions labeled by manganese and tractography, a so-called 'overlap fraction' (OF), the ratio of overlap between those two regions to the tractography-labeled region, was calculated. The OF for three tracts (i.e., corticocortical, corticothalamic and corticonigral tracts) ranged from 0.59 to 0.98, which indicated the reliable detection of these pathways.

In contrast to experiments performed at clinical spatial resolution (i.e., on the order of a mm), another validation study focused on a scale of tens of microns by comparing cellular-level diffusion tensor microscopy and histology [55]. **Flint** *et al*. used a prototype microsurface coil (Bruker Inc., [56, 57]) to perform DTI at a resolution of $15\,\mu m$ on excised pieces of rat/pig spinal cord and compared the FACT derived in-plane tract map to the corresponding Nissl-stain histology. The fiber overlap fraction in rat/pig tissue was high, between 84%-100%.

Although the agreement between DTI tractography-based fiber bundles and the main course of corresponding white matter is encouraging, white matter projections to grey matter regions—corticocortical connectivity—presents more challenges to DTI tractography. In the study of **Johansen-Berg** *et al*., the human thalamus was parcellated based on the probability of connections (inferred from probabilistic diffusion

tractography [44]) to predefined cortical regions. Further, the volumes of the thalamic parcels were associated with histological volumes obtained from a cytoarchitectonic atlas [58]. The resulting associations were 0.71 and 0.70 for the two hemispheres respectively, which were interpreted as high correlations. **Klein** *et al*. explored the reproducibility, generalizability and validity of DTI tractography-based localization in four cortical areas (i.e. SMA, pre-SMA, Brodmann's area 44 and 45) across human subjects, timepoints as well as scanners, and validated results against fMRI and post-mortem cytoarchitectonic data [59]. The final reproducibility across modalities, clustering methods, scanners, timepoints, and subjects was in the order of 80-90%, which indicated that diffusion tractography can reproducibly parcellate the human cortex. Recently, **Stephan** *et al*. implemented a connectivity database – the 'Collation of Connectivity data on the Macaque brain' (CoCoMac, cocomac.org) which contains information on substantial parts of the corticocortical network [60]. **Hagmann** *et al*. employed the CoCoMac data to derive an anatomical connection matrix (composed of 'known present', 'unknown' and 'known absent' entries) and compared this to a connectivity matrix derived from diffusion spectrum imaging (DSI) data. They found that 78.9% of all DSI fibers were identified in positions where connections had been identified and recorded in CoCoMac [61]. This is one of the few studies related to DSI corticocortical validation; however, its limits are obvious: 1) it only provided positive predictive value instead of correlation, due to the lack of detailed information (e.g., fiber density or distribution) on corticocortical connections in the CoCoMac database; 2) DSI is not feasible for clinical use currently.

To the best of our knowledge, DTI-tractography-based corticocortical connectivity

has not been rigorously validated in previous work. Our first aim is to assess the accuracy of DTI tractography as a measure of corticocortical connectivity. Among the various available methods (i.e., gross dissection, histological tracers, MR-visible tracer and functional imaging) for obtaining 'gold standard' connectivity, histochemical tracers are preferable because of their fine-scale labeling (compared to gross dissection), proven specificity (compared to the MR-visible tracer) and direct visualization of tracts (compared to functional imaging). Among a number of histological tracers, BDA is a good choice because of its detailed labeling and bidirectional transport capability [62]. Since BDA-labeled fibers can only be investigated after sacrifice and post-processing, *ex vivo* DWI scans provide the best data acquisition strategy. Thus we will study histological and DTI tractography-derived corticocortical connectivity in an animal model *ex vivo* and quantitatively evaluate the histology-tractography association based on regional and voxelwise analyses.

Based on the results of previous validation studies, DTI tractography is not expected to be a perfect predictor of anatomical white matter pathways or corticocortical connectivity. Thus it is also important to quantify the disagreement between tractography-derived pathways and histological labels and to investigate the reasons (i.e. crossing fibers, bending fibers, model fitting errors, see [63] for review) for the disagreement. The second part of this work will emphasize the limitations of tractography, to improve our ability to anticipate tracking errors and improve tractography methods in a more effective way.

CHAPTER III

VALIDATION OF DTI TRACTOGRAPHY-BASED MEASURES OF PRIMARY

MOTOR AREA CONNECTIVITY

3.1 Introduction

Diffusion tensor imaging (DTI) is a noninvasive method to characterize the microstructure of biological tissue [1]. It is based on measurements of the mean squared displacement of water molecules along the predetermined directions, estimated from the signal decay in a pulsed gradient spin echo acquisition [16]. Water diffusion is anisotropic in many tissues, especially in fibers of tightly packed, parallel axons [18] in brain white matter. Hence, DTI serves as a sensitive probe of axonal fiber orientation [19]. Based on these concepts, white matter pathways can be reconstructed by tracking the inferred axonal orientations step by step (with voxel or subvoxel step size) from seed points. Deterministic tracking algorithms [20-24] construct a unique path from each seed point whereas probabilistic algorithms [25, 43, 54, 64, 65] generate multiple possible paths from each seed point. Both families of tractography algorithms have become valuable research tools for the *in vivo* study of neuronal tissue morphology, pathway location, and other properties which directly relate to neuropsychiatric/neurologic disorders [8], brain organization and development [10, 11].

Among many potential applications of DTI tractography, mapping anatomical

connectivity [66] has attracted the attention of many neurologists, neuroscientists and psychiatrists, since knowing the network structure within and between brain regions is a fundamental prerequisite for understanding mechanisms behind brain functions and dysfunctions. Early experimental methods to reveal connectivity employed gross dissection [28] and neural degeneration procedures [29-31]. More recent experiments exploit neural tracers, which capitalize on cytoplasmic flow and the axoplasmic transport system [32]. Different tracers such as horseradish peroxidase (HRP), lectins, toxins and their conjugates, fluorescent dyes, dextrans and viruses (for review see [67]) have been used in countless investigations that have contributed valuable descriptions of connectivity in the mammalian brain. These very important studies, however, are highly invasive and require fixed, processed tissue for data analysis, preventing their use for *in vivo* connectivity mapping. The recently introduced manganese technique offers an opportunity to study neuronal connectivity *in vivo* by means of MRI [68], but the technique has several drawbacks that can reduce its applicability, the most important being the potential toxicity of the Mn^{2+} ions.

DTI tractography overcomes the problem of invasiveness, but whether or to what extent it reveals true anatomical connectivity is unclear. A number of well-examined factors, e.g., signal to noise ratio [46] and partial volume effects [69], may degrade the fidelity with which tractography can represent the anatomical connectivity [48]. Hence, the agreement between tractography-derived and anatomical connectivity needs to be evaluated quantitatively. Previous *in vivo* or *in vitro* validation studies [49-51] mainly compare tractography-derived pathways with the 'ground truth' white matter fiber bundles

17

revealed using surgical dissection, neural tracer tracking or MR-visible tracer tracking in different animal models. They demonstrated general agreement in a number of specific bundles between tractography-derived pathways and the 'ground truth'. Besides the morphology of white matter pathways, there is increasing interest in measuring corticocortical connectivity using DTI tractography [66]. However, to the best of our knowledge, such measurements have not yet been rigorously validated.

This chapter aims to assess the reliability/sensitivity/accuracy of DTI tractography as a measure of corticocortical connectivity. For this purpose, we studied histological and DTI tractography-derived corticocortical connectivity in an animal model and quantitatively evaluated the histology-tractography association based on regional and voxelwise analysis.

3.2 Methods

3.2.1 Data acquisition

i)   Tracer injection

The experiment was carried out on a New World squirrel monkey which shares many functional organization and microstructural complexities with the human nervous system, although the cortical surface is less gyrated. The motor cortex, for example, is completely exposed on the brain surface, so it is easily accessible for electrical microstimulation and injection of tracers. Other advantages of New World monkeys are that the cortical connections of the primary motor cortex (M1) are well known from previous studies [70]

and their smaller brains reduce the time of histological processing and anatomical data analysis.

Under general anesthesia using aseptic techniques, a bidirectional tracer, biotinylated dextran amine (BDA; Molecular Probes Inc., Eugene, OR) was injected (as a 10% solution in phosphate buffer) into left hemisphere M1. Pressure injections of BDA were carried out using a 2ul Hamilton syringe. Eight injections (1 μl/site; indicated by the black squares in Figure 3.2-1) were made to cover a large M1 region representing the forearm and identified by intracortical microstimulation (see the stimulation sites labeled 'Fa' in Figure 3.2-1). After each injection, the needle was left in the brain for 5-10 minutes and then retracted stepwise to avoid leakage of the tracer along the needle track. Surgical, microstimulation and injection procedures have been described in detail elsewhere [70]. All used procedures were approved by the Vanderbilt University Animal Care and Use Committee, and followed National Institutes of Health guidelines.

After surgery, the monkey was allowed to recover from the procedure, giving the tracer time to be transported along axons to all regions connected to M1.
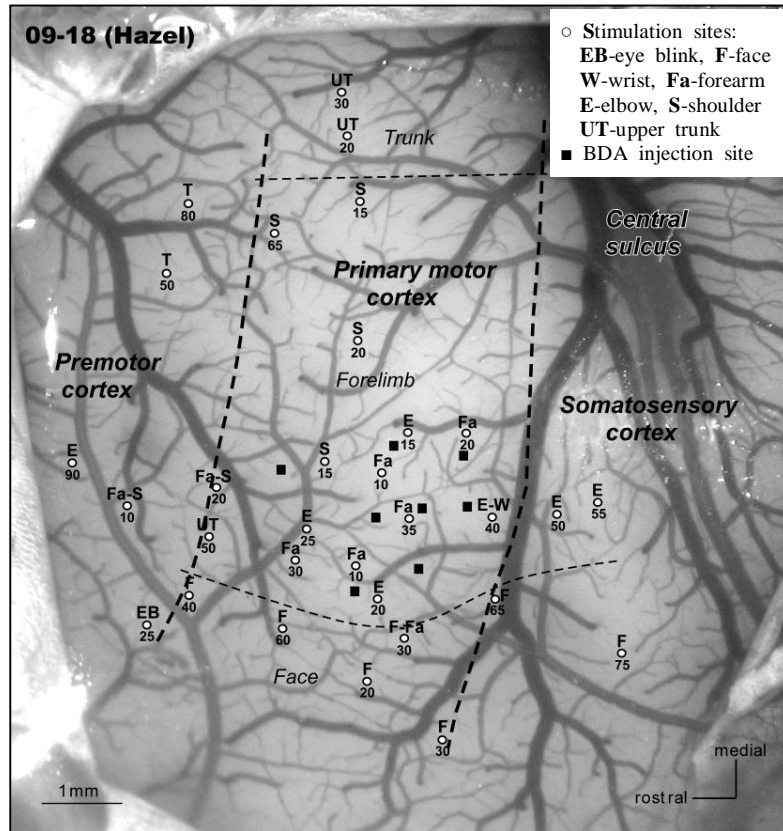
Figure. 3.2-1. Functional map of the primary motor cortex used to guide BDA injections. Results of microstimulation mapping and BDA injection sites overlaid on the exposed lateral surface of the squirrel monkey brain. Cortical sites marked as white dots were stimulated by micro electrode, which evokes body movements of the anesthetized monkey. Letter(s) above each dot indicate the specific elicited movement(s) corresponding to this stimulation site. The number below each dot represents the current threshold (in units of μA) needed to evoke the movement. Thick dashed lines indicate approximate borders of M1, which were identified by the magnitude of threshold (thresholds lower than approximately 40 μA were used to infer the M1 region). Thin dashed lines indicate approximate borders between M1 body representation areas. Black squares show the BDA injection sites covering the forearm movement representation area.

ii) Ex vivo MRI data acquisition

One week after surgery, the monkey was given a lethal dose of barbiturate, and

20

perfused through the heart. All blood was rinsed out with physiological saline (0.9% NaCl) followed by fixative (4% paraformaldehyde). The brain was removed from the skull and stored in buffered saline overnight. The next day, the brain was scanned on a 9.4 Tesla, 21cm bore Varian scanner (Varian Inc., Palo Alto, CA). First, T2-weighted structural images were acquired by running a standard gradient echo multi-slice (GEMS) sequence with full brain coverage (TR = 963ms, TE = 4ms, flip angle = 20˚, slice gap = 0mm, voxel size = $300 \times 300 \times 300 \, \mu m^3$, data matrix = $128 \times 128 \times 192$, SNR $\approx$ 50). Then diffusion weighted imaging was performed using a pulsed gradient spin echo (PGSE) [16] multishot spinwarp imaging sequence with the same FOV as the structural images (TR = 5.2s, TE = 26ms, number of diffusion gradient directions = 31, b = 0, 1200s/mm^2, voxel size = $300 \times 300 \times 300 \, \mu m^3$, data matrix = $128 \times 128 \times 192$, number of acquisitions = 10, SNR $\approx$ 25, scanning time $\approx$ 50hr). The b value used in this experiment was lower than is optimal for diffusion studies in fixed tissue [71], due to hardware limitations. A low b value decreases the available diffusion contrast-to-noise ratio (CNR) in the image data, which has the same effect as higher image noise. To compensate for this shortcoming, we extended the scan time to 50 hours, which yielded a CNR comparable to *in vivo* human studies (equivalent to an *in vivo* study with mean diffusivity = 0.7×10^{-3} mm^2/s and SNR $\approx$20).

iii) Block/micrograph data acquisition

Following MRI scanning, and before sectioning, the entire brain was placed in 30% sucrose for cryoprotection. Two days later the brain was cut serially on a microtome in a coronal plane to produce 50μm thick frozen sections. All sections were collected in the

phosphate buffer, but prior to cutting every third section (i.e., at 150μm intervals), the frozen tissue block was photographed using a Cannon digital camera (image resolution=50μm/pixel, image size=3330×4000pixels, number of images=286), rigidly mounted above the microtome to facilitate intermodality image registration (shown in figure 3.2-2B).
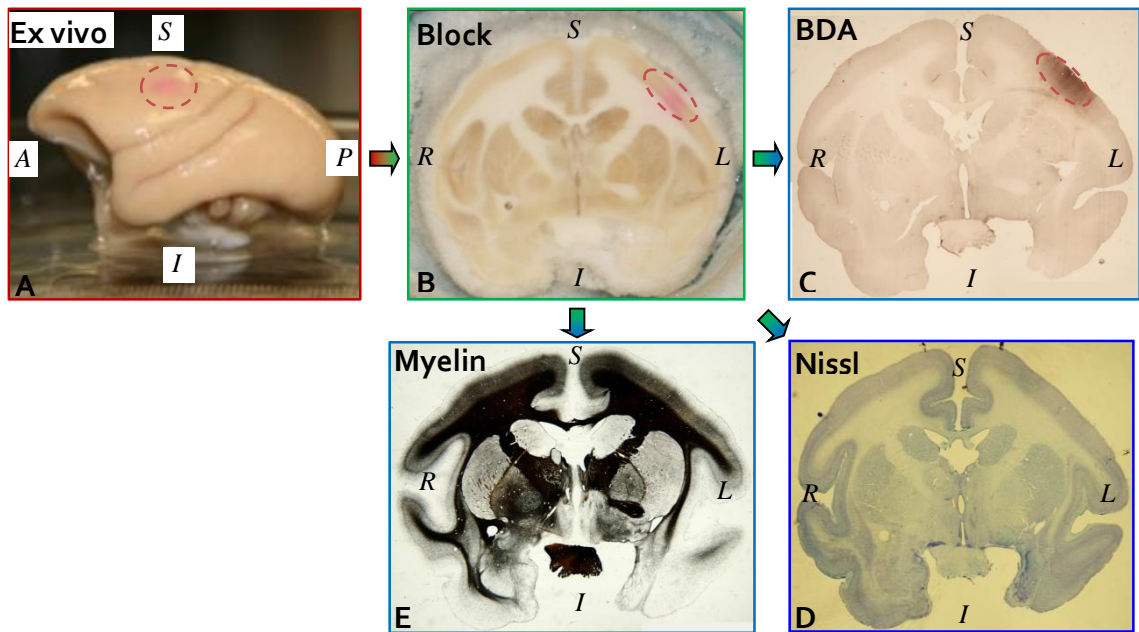
Figure 3.2-2. Overview of anatomical section acquisition after the MRI scan. (A) The left lateral view of the extracted brain with the surface of the injection region outlined with a pink dashed ellipse. The brain was frozen and sectioned coronally as in (B) – a photograph of the block face with the injection region indicated by the pink dashed ellipse. Every sixth section was processed for BDA-the brown color shown in (C) – the BDA stained tissue section with the injection region indicated by the pink dashed ellipse. One series of sections was Nissl stained as shown in (D) to acquire cytoarchitectural information and another series of sections was stained for myelin in (E) to visualize all the axons.

Sections were divided into six series. Every sixth thin section was processed for BDA

histochemistry [62], producing a series of 74 sections covering all regions connected to M1. These sections were photographed under 0.5X magnification using a Nikon DXM1200F digital camera mounted on a Nikon E-800 microscope (image resolution=7 μm/pixel, image size=3840×3072 pixels), shown in figure 3.2-2C. More than one photograph was needed to cover the entire section. Those component photographs were merged into a panoramic micrograph using Adobe Photoshop CS3 (San Jose, CA) and the background of each panorama was extended to a net image size of 6660×6660 pixels. The resulting stack of images defined a "standard micrograph space" which is the target space of all higher resolution microscopic data.

One adjacent series of sections was stained for Nissl substance, shown in figure 3.2-2D, to identify the cytoarchitectonic borders of M1 and other cortical regions connected to M1. Another adjacent series of sections was stained for myelinated fibers, shown in figure 3.2-2E, to visualize all the axons distributed throughout the white matter tissue. The remianing sections were used for other purposes.

3.2.2 Data processing

i) *Micrograph-space to DTI-space registration*

High resolution micrograph (higher than 0.5X) were registered to the DTI space using a multi-step procedure, illustrated by figure 3.2-3. First, every high resolution BDA-labeled micrograph was down-sampled (to 256×256 pixels) and registered to the corresponding low resolution micrograph (256×256 pixels) using a 2D rigid transformation. Second, every low resolution micrograph of BDA-labeled sections (256×256) was registered to the downsampled photograph of the corresponding tissue

block (256×256) using 2D affine transformation followed by 2D non-rigid transformation semi-automatically calculated via the Thin-Plate Spline algorithm [72]. Next, all the downsampled block micrographs were assembled into a block volume and all the non-diffusion weighted MRI images were similarly stacked into a DTI volume. Then the block volume was registered to the DTI volume using a 3D affine transformation followed by 3D non-rigid transformation automatically calculated via the Adaptive Bases Algorithm [73]. The multi-step registration described here was very similar to the registration procedure validated in an early study [74], which showed that the accuracy of the overall registration was around one MRI voxel size (0.3mm). The deformation fields produced by all the above registration steps were saved in order to transfer other data acquired from the same micrograph space into DTI space.
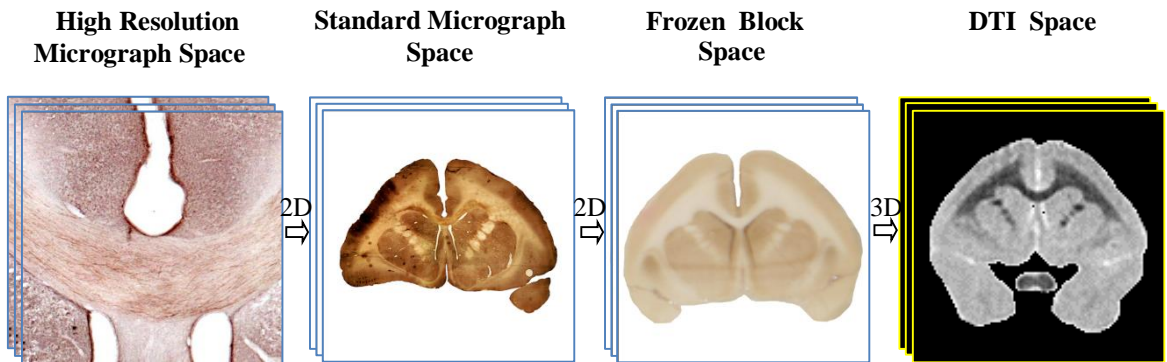
Figure 3.2-3. Schematic overview of the registration strategy. The spatial transformation between the high resolution micrograph space and DTI space was calculated in multiple steps: high to low resolution micrograph, to tissue block and then to DTI volume.

ii)　　*Fiber and density distribution map (DDM) reconstruction*

Our ultimate goal in this part of the study was to reconstruct histological and DTI-tractography-based fiber density distribution maps (DDMs) in DTI space and render them

24

on the white-grey matter (WGM) interface. Prior to calculating DDMs, we reconstructed the 3D WGM interface in DTI space: the T2w image volume was rigidly registered to the DTI volume; white matter was segmented using a variational level set approach [75] on the aligned T2w images; the 3D outline of white matter was extracted to generate triangle meshes representing the WGM interface. In addition, the BDA-injection region and different cortical projection regions were segmented manually in the standard micrograph space based on architecture revealed by Nissl-stained sections [70] and then transferred to DTI space.

To resolve each individual BDA-labeled fiber, 4X micrographs (0.87 μm/pixel) covering the WGM boundary were acquired using a Nikon D1R1 digital camera mounted on a Nikon MULTIZOOM AZ100M microscope. The BDA-labeled fibers were segmented by a series of morphological processes: top-hat filtering was performed to correct uneven illumination, global thresholding was applied to extract fibers, and a set of statistical properties (e.g., area of object, ratio of object perimeter to area, etc.) of each extracted object were calculated and used to remove the non-fiber objects. For each micrograph, we manually selected the points along the WGM boundary and fit these points to a curve with 6 pixels (~5 μm) width to represent the histological WGM boundary. Segmented fibers that overlapped the fitted boundary were extracted automatically. The centroids of these overlapping fibers were rigidly transferred to the standard micrograph space, slice by slice.

Next, the standard size micrograph (6660×6660 pixels) was divided into 256×256 square units and the number of centroids in each unit area, $n_{i,j}$ (i,j = 1,2,…,256), was

25

determined. These $n_{i,j}$ values served as the intensity of the 2D DDM. The DDMs were transferred from micrograph space to block space then to DTI space using the deformation field associated with the registration procedure described earlier (see *i)* in section 3.2.2). Immediately following each spatial transformation step, the Jacobian matrix of the corresponding deformation field was calculated and then used to compensate the density change caused by the raw geometric transformation. Finally, to facilitate visualizing the density information in 3D, we mapped these grey-matter-distributed densities onto the WGM interface in 3D DTI space. Thus, ideally, the value of a certain voxel on the WGM interface in 3D DTI space represented the number of BDA-labeled fibers whose centroids were located on the WGM boundary in high resolution micrograph space.

To identify the locations of BDA-labeled somas in the micrographic volume, we exhaustively plotted the centers of these somas and the outline of the brain tissue for each BDA-labeled section under the 6.3X objective of a Zeiss microscope equipped with the vector graphing software Igor Pro 2.0 (Wavemetrics, Inc., Lake Oswego, OR). Using Canvas 11 (ACD Systems, Victoria, British Columbia, Canada), each vector graph was converted to a bitmap image with resolution high enough to resolve any two adjacent soma markers. The bitmap image was rigidly aligned with the 0.5X micrograph of the corresponding BDA-labeled section by matching the outline of the brain tissue and then was cropped into a standard size image. Next, each labeled soma was segmented by simple thresholding and the centroid of the soma was extracted automatically; the procedures (including gridding, counting, and calculating, then transferring and

compensating the DDM) were similar to those for processing BDA-labeled fiber data. Finally, we mapped these grey-matter-distributed densities onto the WGM interface in 3D DTI space: the density value of every grey matter voxel was added to the closest voxel (in 3D) located on the WGM interface. Thus, ideally, the value of each voxel at the interface was the sum of the number of BDA-labeled somas located vertically (i.e., normal to the surface) beyond this voxel.

DTIStudio [76] software was used to perform tensor fitting and fiber tracking (using the FACT algorithm, [21]) over the whole brain (tensor fitting method: standard linear-fitting; tracking parameters: start fractional anisotropy (FA) = 0.1, stop FA = 0.2 and stop angle = 70˚). Streamlines penetrating both of the following two ROIs were selected: (i) the BDA-injection region transferred from the micrograph space and (ii) the WGM interface just underneath (i). The above deterministic tracking scheme is referred to as the 'DS' scheme below. The DDM for this tracking method was produced by counting the number of the streamlines passing through or terminating within the voxels at the WGM interface. In addition, the streamline terminals distributed within the cortical regions connected to M1 were also mapped onto the interface and then counted for each interface voxel to produce a DTI 'streamline terminal' DDM.

Probabilistic fiber tracking were performed with FMRIB's Diffusion Toolbox (FDT) v2.0 from the commonly-used FMRIB's Software Library (FSL, http://fmrib.ox.ac.uk/fsl). First, the *bedpostx* command was run to calculate the distributions of diffusion parameters at each brain voxel using the Markov Chain Monte Carlo sampling method [25], with the automatic relevance determination (ARD) weight assigned to 1 (default)

and 0.5, respectively. The *probtrackx* command was used to generate probabilistic streamlines (using the following parameters: sample number=10000, curvature threshold=0.2, modified Euler streamlining=on, step length=0.1 mm and distance correction=on. The BDA-injection region was used as the seed mask, the WGM interface underneath the injection region as the waypoint mask and the grey matter mask (excluding the injection region) as the termination mask. These probabilistic tracking schemes are referred to as 'FSL1' (ARD weight=1) and 'FSL2' (ARD weight=0.5), respectively. The voxel value in the resulting dataset represents the number of streamline samples passing through this voxel times the expected length of these samples. The probabilistic-tractography-derived DDM was generated just by keeping the values of those voxels located at the WGM interface and setting the remaining voxels to zero. Again, the DDM were finally rendered on the WGM interface in 3D DTI space.
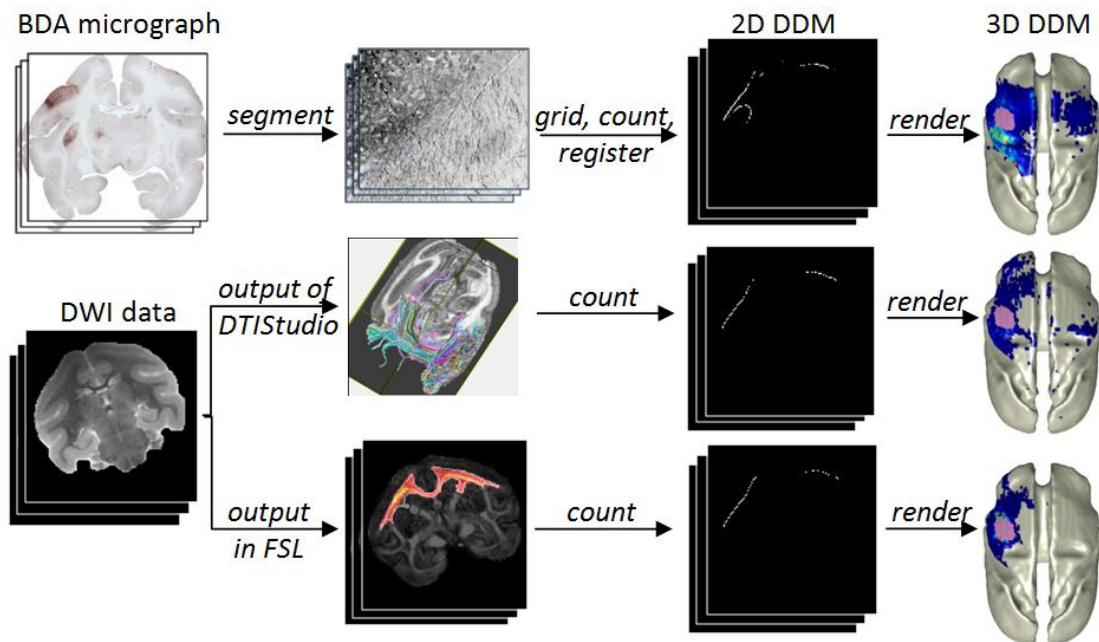
Figure 3.2-4. Schematic workflow for production of density distribution maps (DDMs). The first row shows how the BDA-labeled fiber DDM was generated. The second and

third rows show how deterministic and probabilistic streamline DDMs, respectively, were created. The general processes for each step are shown in italics. The DDMs will be used for further analysis and comparison.

3.2.3 Data analysis

i)   *Connectivity Correlation Analysis*

When the number of DTI-tractography-derived streamlines was proposed as a measure of corticocortical connectivity [66], one of the hypotheses was that the number of streamlines is **proportional** to the number of axons connecting cortical regions. To test this hypothesis for inter-regional connectivity, the numbers of BDA-labeled fibers (N_B) passing into cortical ROIs and the numbers of DTI streamlines (N_D) going into the same ROIs were quantified. These data were fit to a linear model:

$$N_D = a + bN_B + e,$$
(3.2-1)

where a and b are, respectively, the estimated intercept and slope of the regression line, and e is the error term. If a=0 lay within the 95% of confidence interval of the intercept, then the data were fit to a second tier linear model with intercept a equal to zero:

$$N_D = b'N_B + e'.$$
(3.2-2)

The Pearson's correlation coefficient of the fit, r, was calculated to indicate the degree of correlation between tractography and histology fiber data.

To verify the hypothesis in the case of intra-regional connectivity, we calculated the Pearson's correlation coefficient, r_p, between tractography and histology fiber DDMs within each cortical projection region on a voxel-by-voxel basis:

$$r_p = \sum_{i=1}^{n}(B_i - \bar{B})(D_i - \bar{D}) / \left\{ \sqrt{\sum_{i=1}^{n}(B_i - \bar{B})^2} \sqrt{\sum_{i=1}^{n}(D_i - \bar{D})^2} \right\}, \qquad (3.2\text{-}3)$$

where B_i and D_i are, respectively, the numbers of BDA-labeled fibers and DTI streamlines, distributed in the ith voxel located at the WGM interface directly underneath this projection region, n is the total number of these voxels, and the bar represents the mean.

The original seed region covered the grey matter in the injection region, but it was found that DTI tractography was more effective when the seed region was intentionally extended one or two voxels into the white matter under the WGM interface. To examine the effect of extending the depth, d_w, of the seed region into the white matter, we calculated all the correlations using seed masks with d_w=0, 1 and 2 voxels (= 0, 0.3 and 0.6mm).

In addition, since obtaining the DDM of BDA-labeled somas was less time-consuming, we studied the feasibility of using soma number to represent histological connectivity. We therefore calculated the relationship between numbers of BDA-labeled somas and BDA-labeled fibers across all projection regions. We also calculated the association between numbers of BDA-labeled somas and numbers of DS streamline-terminals across all the projection regions.

ii) *Variability Analysis --Bootstrap*

Due to limited scanning time and the desire to acquire more diffusion directions instead of multiple repetitions of the same directions, only one single set of *ex vivo* DWI data was obtained during the two day scanning measurement. To estimate the variability

of density distribution of the DTI tractography-derived fibers, the residual bootstrap [77] and wild bootstrap were implemented for the basic single tensor model and ball-and-stick model [25, 26] respectively, because these two approaches are applicable to single acquisition DWI data and were reported to have small biases and overall errors compared to other resampling approaches [77].

Basically, the residual bootstrap is a resampling technique applied to the linear regression model, where the regression residuals are assumed to have similar distributions and therefore can be freely resampled among them without stratification [77]. The details of the residual bootstrap procedure on the single tensor model are described as follows.

The diffusion signal, S, in single tensor model is modeled by

$$\ln\big(S(\boldsymbol{g}_i)\big) = \ln(S_0) - b\boldsymbol{g}_i^T \boldsymbol{D} \boldsymbol{g}_i, \ \text{with } i = 1,2,\dots,N, \tag{3.2-4}$$

which can be structured into linear regression form

$$\boldsymbol{y} = \boldsymbol{X}\boldsymbol{\beta} + \varepsilon, \tag{3.2-5}$$

with

$$\boldsymbol{y} = [\ln(S(\boldsymbol{g}_1)), \ln(S(\boldsymbol{g}_2)), \dots, \ln(S(\boldsymbol{g}_N))]^T,$$

$$\boldsymbol{\beta} = [D_{xx}, D_{yy}, D_{zz}, D_{xy}, D_{xz}, D_{yz}, \ln(S_0)]^T,$$

design matrix

$$\boldsymbol{X} = -b \begin{bmatrix} g_{1x}^2 & g_{1y}^2 & g_{1z}^2 & 2g_{1x}g_{1y} & 2g_{1x}g_{1z} & 2g_{1y}g_{1z} & 1 \\ \vdots & \vdots & \vdots & & \vdots & \vdots & \vdots & \vdots \\ g_{Nx}^2 & g_{Ny}^2 & g_{Nz}^2 & 2g_{Nx}g_{Ny} & 2g_{Nx}g_{Nz} & 2g_{Ny}g_{Nz} & 1 \end{bmatrix},$$

and error terms $\varepsilon = [\varepsilon_0, \varepsilon_1, \dots, \varepsilon_N]^T$. The weighted least squares (WLS) estimate of $\boldsymbol{\beta}$ was calculated by

$$\widehat{\boldsymbol{\beta}} = (\boldsymbol{X}^T \boldsymbol{W} \boldsymbol{X})^{-1} \boldsymbol{X}^T \boldsymbol{W} \boldsymbol{y}, \qquad\qquad (3.2\text{-}6)$$

in which the weighting matrix $\boldsymbol{W} = diag(\widehat{\boldsymbol{S}}_g^2)$. Here $\widehat{\boldsymbol{S}}_g$ is the diffusion signal estimated by ordinary least square (OLS) fitting: $\widehat{\boldsymbol{S}}_g = \exp(\mathbf{X}(\boldsymbol{X}^T \boldsymbol{X})^{-1} \boldsymbol{X}^T \boldsymbol{y})$. Then the WLS fitted log measurements $\widehat{\boldsymbol{\mu}} = \boldsymbol{X}\widehat{\boldsymbol{\beta}}$ were used to compute the residual vector $\boldsymbol{e} = \boldsymbol{y} - \widehat{\boldsymbol{\mu}}$. Each raw residual $y_j - \hat{\mu}_j$ was modified to have constant variance by

$$r_j = \frac{y_j - \hat{\mu}_j}{w_j^{-1/2}(1 - h_j)^{1/2}}, \qquad\qquad (3.2\text{-}7)$$

where the weighting factor w_j is the jth diagonal element of $\boldsymbol{W}$ and the leverage value h_j is the diagonal element of the matrix $\boldsymbol{H}$ given by $\boldsymbol{H} = \boldsymbol{X}(\boldsymbol{X}^T \boldsymbol{W} \boldsymbol{X})^{-1} \boldsymbol{X}^T \boldsymbol{W}$. The final residual bootstrap resampling is defined by

$$y_j^* = x_j \widehat{\boldsymbol{\beta}} + w_j^{-1/2} \varepsilon_j^*, \qquad\qquad (3.2\text{-}8)$$

where y_j^* is jth element of resampled log measurements, x_j is the jth row of $\boldsymbol{X}$, and ε_j^* is randomly resampled with replacement from the set of centered modified residuals $r_1 - \bar{r},\ r_2 - \bar{r},\ ...,\ r_N - \bar{r}$.

One bootstrap sample set $\boldsymbol{y}_j^* = [y_1^*, y_2^*, ..., y_N^*]^T$ led to one signal sample set $\boldsymbol{S}_j^* = [S_1^*, S_2^*, ..., S_N^*]^T$, with

$$S_j^* = \exp(y_j^*), \qquad\qquad (3.2\text{-}9)$$

in the resampled DWI dataset.

In our analysis of single tensor methods, 30 independent sets of resampled DWI signals were acquired using the above steps. Then those sample sets were used to calculate tensors, track fibers and then compute the density distribution of fibers using the tracking schemes described in the next section.

With regard to the ball-and-stick model, we specified two sticks in our experiments, so the model becomes:

$$S_i = S_0(1 - f_1 - f_2)\exp(-b_i d) + \sum_{k=1}^{2} f_k \exp(-b_i d \boldsymbol{g}_i^T \boldsymbol{R}_k \boldsymbol{A} \boldsymbol{R}_k^T \boldsymbol{g}_i), \qquad (3.2\text{-}10)$$

where S_i is the predicted signal, S_0 is the non-diffusion-weighted signal, d is the diffusivity, b_i is the b-value applied along the diffusion gradient direction, $\boldsymbol{g}_i$, and f_k and $\boldsymbol{R}_k \boldsymbol{A} \boldsymbol{R}_k^T$ are the fraction of signal contributed by and the anisotropic diffusion tensor along, the kth fiber orientation (θ_k, φ_k). The matrix $\boldsymbol{A} = \begin{pmatrix} 1 & 0 & 0 \\ 0 & 0 & 0 \\ 0 & 0 & 0 \end{pmatrix}$ and $\boldsymbol{R}_k$ rotates $\boldsymbol{A}$ to (θ_k, φ_k).

For this ball-and-stick model, we were able to obtain all the fitted parameters (i.e., $d, \theta_k, \varphi_k, f_1, f_2$) from FSL, so we could calculate the residual along each diffusion gradient direction, change the sign of the residual randomly, and add the new residual back to the predicted signal. The new synthetic signals are the wild bootstrap samples from which we calculated the variability of correlation coefficients for FSL schemes.

3.3 Results

3.3.1 M1-connecting cortices

BDA labeling originating from the forelimb representation area in the M1 cortex reveals somatotopically distributed connections with the ipsi-/contra-lateral supplementary motor areas (iSMA/cSMA); ipsi-/contra-lateral anterior cingulate cortex (iAC/cAC); ipsi-/contra-lateral premotor cortex (iPM/cPM); ipsilateral M1 excluding the injection region

(iM1ex); contra-lateral M1 (cM1); ipsi-/contra-lateral anterior parietal cortex (iPA/cPA); ipsi-/contra-lateral posterior parietal cortex (iPP/cPP); anterior part of upper bank of ipsi-lateral lateral sulcus—a combination of parietal ventral and rostral areas (iPVR); posterior part of upper bank of ipsi-/contra-lateral lateral sulcus—secondary somatosensory cortex (iS2/cS2). Labeling of ipsi-/contra-lateral prefrontal cortex (iPF/cPF) and contra-lateral PVR (cPVR) were not observed in this case. All the above listed regions served as our ROIs. The borders of these ROIs were identified based on their cytoarchitectural features seen in Nissl preparations [78]. Figure 3.3-4A shows those ROIs as well as the BDA injection region (IR) mapped on the WGM interface in the DTI space.

3.3.2 Detection and counting of cross-interface BDA-labeled fibers

Figure 3.3-1 illustrates the pipeline of semi-automatic detection of cross-interface BDA-labeled fibers in the high resolution micrograph space. The WGM boundary (yellow curve shown in figure 3.3-1C) was estimated by fitting a series of manually-placed markers (red dots in figure 3.3-1B) on 4X micrographs covering a specific ROI (the blue frame in figure 3.3-1A shows the ROI location in the brain). Interface-crossing fibers (fibers with color contours shown in figure 3.3-1D) were detected automatically by performing an "AND" operation on the fiber and the boundary binary masks. Locations of the interface-crossing fibers were defined by the centroids of these fibers; meanwhile the number of interface-crossing fibers was counted (red numbers in figure 3.3-1D). It was verified that shifting the WGM boundary towards white matter or grey matter by 50 pixels (~44 μm) did not significantly change the number of interface-crossing fibers. The

34

deviation of semi-automated counting from manual counting as the "gold standard" was also studied. Four to five sections for each ROI were randomly drawn for verification. The deviations for all the ROIs were in the range of 3% -5%.
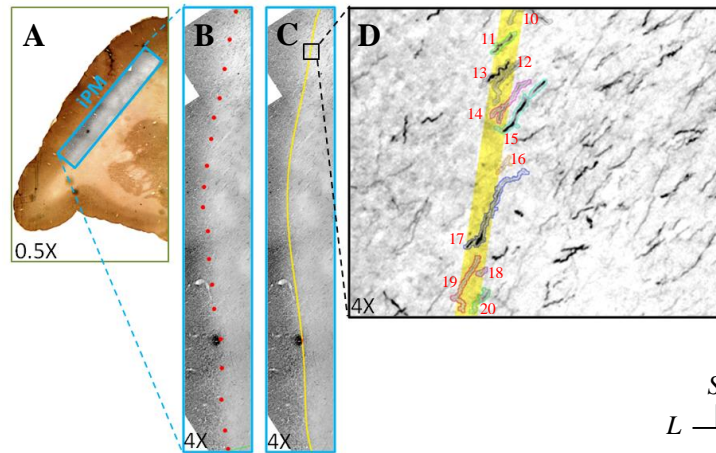
Figure 3.3-1. Pipeline for detecting and counting interface-crossing BDA-labeled fibers. Acquired grayscale 4X micrograph (B) covering a specific ROI (iPM in this example), aligned to the corresponding 0.5X micrograph (A) in standard micrograph space. (B) shows manually placed markers (red dots) used to identify the WGM boundary. (C) shows the fit of the markers to a continuous curve (yellow). (D) shows segmented BDA-tagged fibers (those with color contours) that touch the WGM boundary along with their numerical index (red numbers beside the fibers).

3.3.3 Tensor fitting results

The DWI data were fitted to single-tensors using DTIStudio. The primary diffusion direction and FA were calculated in each voxel. Figure 3.3-2 shows a color-coded map of primary diffusion direction and the FA scalar map of the same coronal slice.
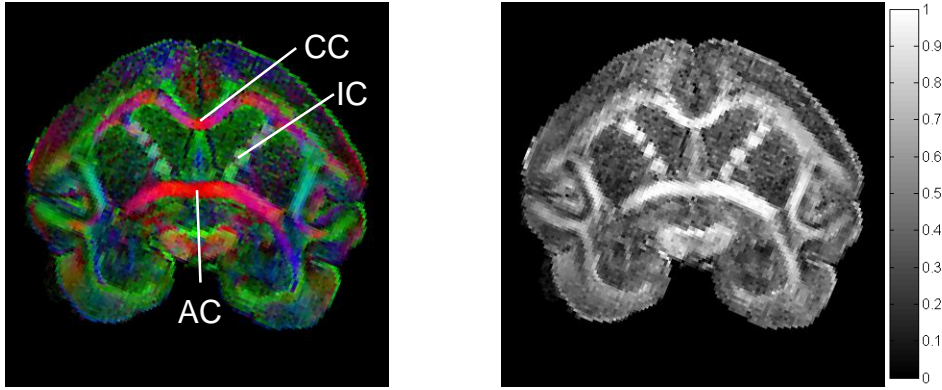
Figure 3.3-2. Maps of color-coded primary diffusion direction (red = Right/Left, green = Anterior/Posterior, and blue = Superior/Inferior) and scalar FA value. (CC - corpus callosum, IC - internal capsule and AC - anterior commissure).

3.3.4 Correlation of inter-ROI connectivity strength

To test the hypothesis that the number of streamlines, N_D, connecting two cortical regions is proportional to the number of anatomical fibers, N_B, connecting those regions, we identified the number pair for connections between M1 and each ROI and plotted them in figure 3.3-3 as well as displayed them as connectivity backbones, shown in figure 3.3-4. The number pairs lying on the horizontal axis (N_D=0) and vertical axis (N_B=0) in figure 3.3-3 reveal false negative and false positive connections, respectively. Approximately 75%-98% of streamlines reached the true positive ROIs for our nine predefined regions. By performing linear regression based on the model in Eq. 3.2-1 and calculating the 95% confidence interval for the intercept, we found that all nine confidence intervals included the origin. Therefore, we fit to the constrained linear model in Eq. 3.2-2 to generate the regression lines in figure 3.3-3. The Pearson's correlation coefficient r and corresponding p value for each case are shown in Table 3.3-1. Because the data span many orders of magnitude, the Pearson's correlation coefficient

(and corresponding p) is dominated by the largest values. For this reason, we also calculated the Spearman rank correlation coefficient, r_s, and corresponding p value, which depends only on the relative rank of connection strengths measured by the two methods. The values of r_s in Table 3.3-1 are quite low and do not reach statistical significance. To focus on the strongest connections, we chose the ten regions with the highest number of BDA-labeled fibers (i.e., number of BDA fibers > 100) and calculated the Spearman rank correlation coefficient, $(r_s)_{10}$, and corresponding p value for this subset of the data.

Comparison across the three tractography schemes with $d_w = 0$ or 0.3mm (distance of zero or one voxel from the WGM interface) indicates that the linear correlations for the two probabilistic schemes are significantly lower than those of the deterministic scheme. When $d_w = 0.6$mm, however, the linear correlations for these three schemes are quite similar and deterministic tractography gave no false negative results. In addition, under any fixed d_w, the FSL1 and FSL2 schemes have similar r value, but FSL2 has a smaller number of false negative ROIs than FSL1 does.

The influence of d_w on the three tractography schemes, shown in the rows of figure 3.3-3A-C and first six rows of Table 3.3-1 are different. As d_w increases, the number of false negative ROIs decreases except for the FSL2 scheme. For the FSL1 and FSL2 schemes, as d_w increases, the r value increases significantly. For the DS scheme, the r value increases less strongly than for the FSL1 and FSL2 schemes.

The proportional relation between the number of BDA-labeled somas and the number of streamline-terminals, shown in figure 3.3-3D and Table 3.3-1 row 7, is similar to the

relationship between BDA-labeled fibers and streamlines in figure 3.3-3A and Table 3.3-1 row 1, except the number of false negative ROIs were more for the soma-terminals case. The proportional relationship between BDA-labeled soma and fibers, shown in figure 3.3-3E and bottom 2 rows in Table 3.3-1, is statistically significant.

Figure 3.3-4 shows the backbones of the BDA-labeled, DS and FSL2 derived inter-regional connectivity. There are no edges connecting IR to iPF, cPF and cPVR shown in figure 3.3-4A but there are edges between IR to those regions in figure 3.3-4BC, which indicates iPF, cPF and cPVR are false positive regions detected by DS and FSL2 with d_w=0.6mm.
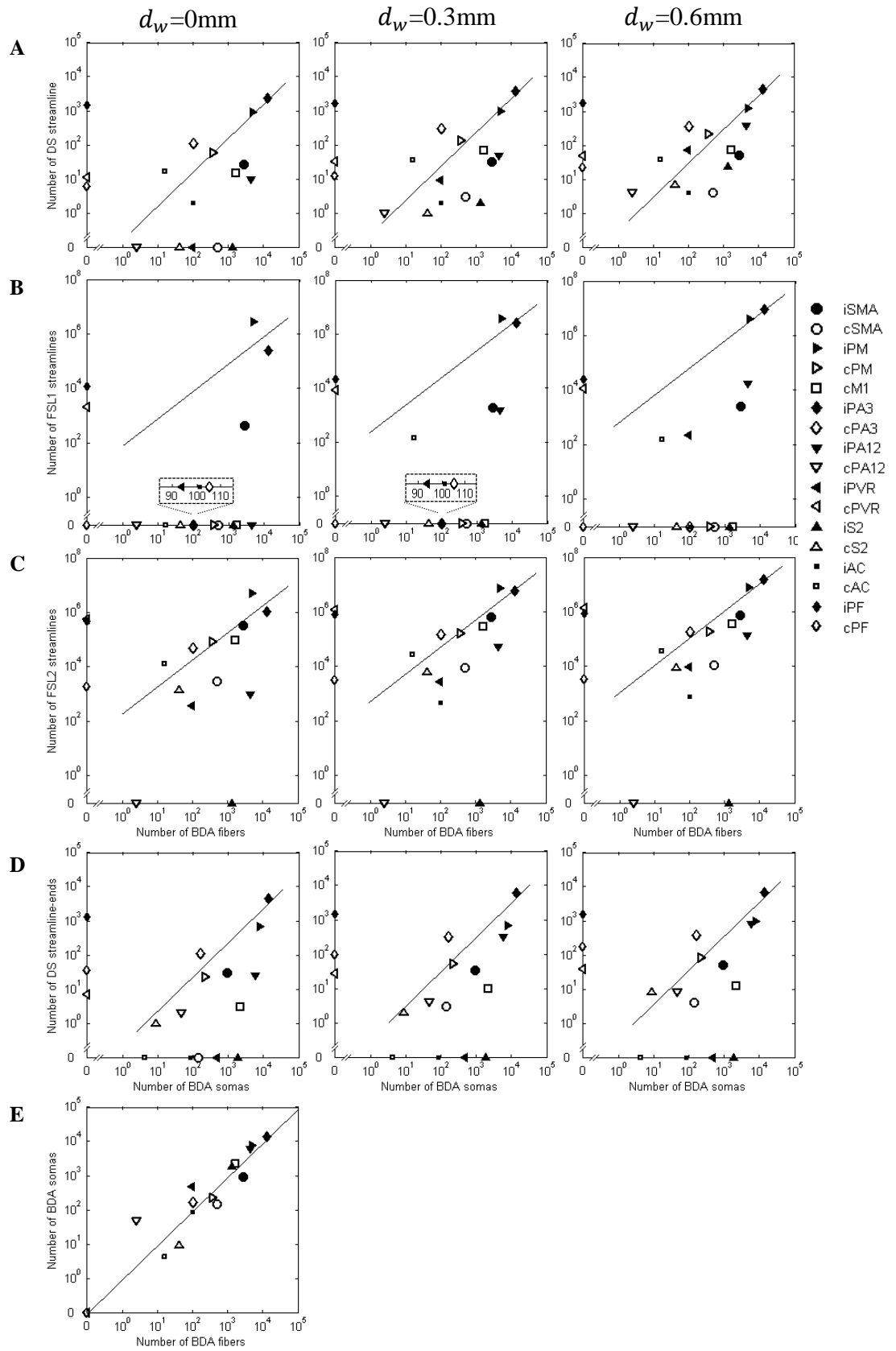
Figure 3.3-3. Relationship between tractography-histology variables as well as histology-histology variables: (A-C) shows tractography-derived streamline vs. BDA-tagged fiber data; (D) shows streamline terminals vs. BDA-tagged soma data; and (E) shows BDA-tagged soma vs. BDA-tagged fiber data. DS (A and D), FSL1 (B) and FSL2 (C) schemes were used to obtain tractography-derived streamlines when d_w is 0, 0.3 and 0.6mm. Proportional relationships were fitted based on least squares regression. The correlation coefficients with corresponding p values of the regressions are listed in Table 3.3-1.
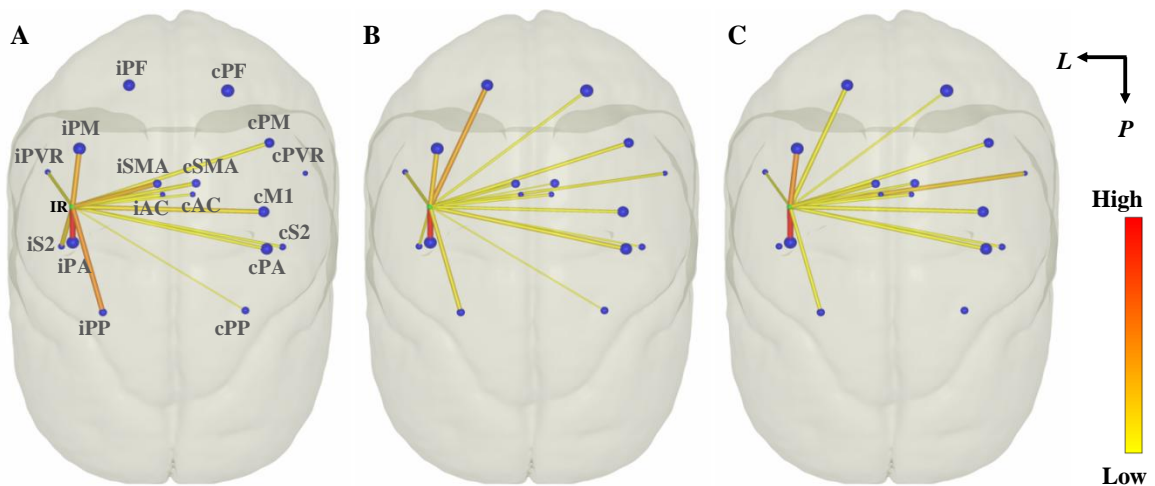
Figure 3.3-4. Dorsal view of the inter-regional connectivity backbones. (A), (B) and (C) show the BDA-labeled fibers (the gold standard), DS and FSL2 derived (d_w=0.6mm) connectivity backbones, respectively. Green and blue nodes indicate the center of mass of the injection and individual projection regions, respectively. The radius of each node is scaled by the square root of the volume of the corresponding region. The thickness of each edge represents the logarithmic connection strength and the color of the edge is coded according to connection weight (strength divided by volume of the projection region).

Table 3.3-1. Pearson's correlation, r, and Spearman's rank correlation, r_s and $(r_s)_{10}$, coefficients with corresponding p values of tractography-histology variables as well as histology-histology variables. Significant correlations are shown in bold.

	$d_w = 0$mm	$d_w = 0.3$mm	$d_w = 0.6$mm
BDA fibers vs. DS streamlines	r **=0.75 (p<0.0005)**	r **=0.82 (p<0.0001)**	r **=0.86 (p<0.0001)**
	r_s =0.30 (p<0.24)	r_s =0.36 (p<0.16)	r_s =0.45 (p<0.07)
	$(r_s)_{10}$=0.44 (p<0.21)	$(r_s)_{10}$=0.49 (p<0.15)	$(r_s)_{10}$**=0.67 (p<0.035)**
BDA fibers vs. FSL1 streamlines	r =0.33 (p<0.10)	r **=0.73 (p<0.0008)**	r **=0.92 (p<0.0001)**
	r_s =0.23 (p<0.38)	r_s =0.27 (p<0.30)	r_s =0.29 (p<0.26)
	$(r_s)_{10}$**=0.74 (p<0.015)**	$(r_s)_{10}$**=0.86 (p<0.0014)**	$(r_s)_{10}$**=0.89 (p<0.0006)**
BDA fibers vs. FSL2 streamlines	r **=0.41 (p<0.03)**	r **=0.75 (p<0.0005)**	r **=0.92 (p<0.0001)**
	r_s =0.25 (p<0.34)	r_s =0.35 (p<0.17)	r_s =0.36 (p<0.15)
	$(r_s)_{10}$=0.61 (p<0.067)	$(r_s)_{10}$**=0.66 (p<0.044)**	$(r_s)_{10}$**=0.66 (p<0.044)**
BDA soma vs. DS streamline-ends	r **=0.80 (p<0.0001)**	r **=0.81 (p<0.0001)**	r **=0.84 (p<0.0001)**
	r_s =0.19 (p<0.47)	r_s =0.23 (p<0.38)	r_s =0.23 (p<0.37)
	$(r_s)_{10}$**=0.63 (p<0.050)**	$(r_s)_{10}$**=0.63 (p<0.050)**	$(r_s)_{10}$**=0.69 (p<0.026)**
BDA fibers vs. BDA soma	r **= 0.97 (p<1.0e-10)**		
	r_s **= 0.95 (p<4.5e-9)**		

3.3.5 Correlation of spatial distributions of connectivity within ROIs

To visualize the spatial distribution of BDA-labeled fibers (or somas) as well as DTI streamlines (or streamline-terminals) from the ROI scale down to the voxel scale, the density distribution of BDA somas, BDA interface-crossing fibers, DTI streamline-terminals and DTI interface-crossing streamlines were rendered on the WGM interface in 3D DTI space (figure 3.3-5). Comparison between figure 3.3-5B and figure 3.3-5C-E indicated that distribution patterns of BDA and DTI fibers (DS and FSL schemes) are

quite different. Likewise, comparison between figure 3.3-5F and figure 3.3-5G exhibits different distribution patterns of BDA somas and DTI streamline-terminals. Table 3.3-2 lists the quantitative evaluation of the agreement: the Pearson's correlation coefficient, r_p, of anatomical and DTI derived distributions in each individual ROI. Overall, the significant linear correlations for all the ROIs were lower than 0.5. The FSL2 scheme provided stronger linear correlations than FSL1 did, but comparable correlations to the DS scheme for most of ROIs. The agreement in iPM is higher than the other projection regions due to higher sensitivity of DTI along this fiber pathway.
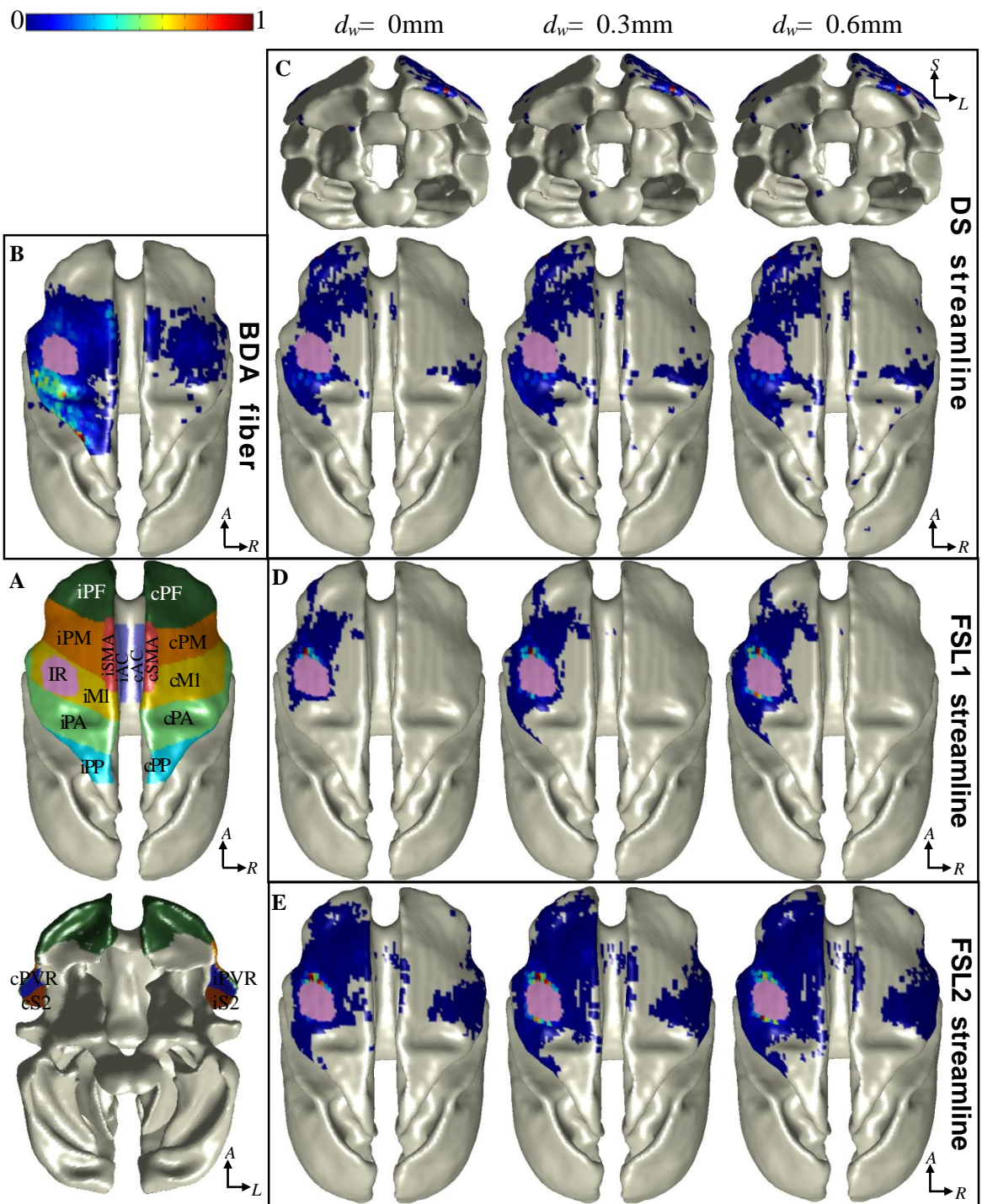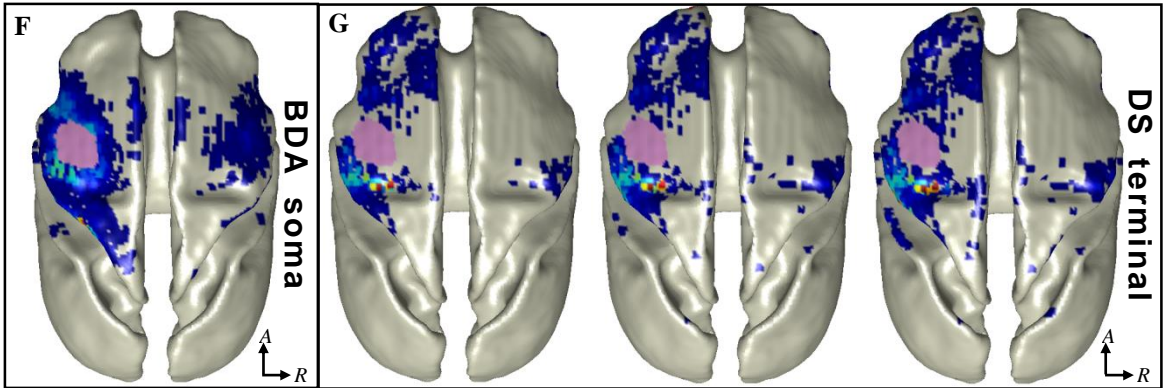
Figure 3.3-5. Dorsal view of 3D fiber density distribution maps (DDMs) rendering on the white-grey matter (WGM) interface. (A) shows territories of all the ROIs and the BDA injection region (upper-dorsal view; bottom-ventral view). (B) shows the BDA fiber DDM and (C-E) show respectively the streamline DDMs using DS, FSL1 and FSL2 tractography schemes (in rows) with different d_w (in columns). (F) shows BDA soma DDM and (G) shows streamline terminal DDMs with different d_w (in columns).

We also investigated whether deeper seed regions could help to achieve better distribution accuracy by increasing the probability that streamlines could bypass crossing fibers directly underneath the WGM interface. Results for d_w=0, 0.3 and 0.6mm for each tractography scheme are shown in rows of Table 3.3-2. For the DS scheme, no significant trend in correlations with BDA connectivity was found as d_w increased (p>0.99 in one-way ANOVA test). For the FSL1 and FSL2 schemes, correlations for ipsilateral ROIs did not have statistically significant differences (p>0.75 and p>0.72) although they seemed to have subtle increasing trends as d_w increased. No test was performed for contralateral ROIs, since the correlations were weak in those cases.

Table 3.3-2. Pearson's correlation coefficients, r_p, (with p values) of histological and DTI tractography-derived distributions for all the projection regions. Significant correlations are shown in bold, and correlation results for tagged somas are shown in italics.

d_w	Group		iAC	iSMA	iPM	iM1	iPA	iPP	iPVR	iS2	cAC	cSMA	cPM	cM1	cPA	cPP	cPVR	cS2
= 0 mm	BDA-DS fibers	r_p	-.02	.01	**.35**	**.22**	**.41**	**.18**	-.00	.00	-.02	-.00	-.05	-.04	**.22**	.00	-.00	-.00
		p	.64	.86	.00	.00	.00	.00	1	1	.65	1	.26	.32	.00	1	1	1
	BDA-FSL1 fibers	r_p	.00	**.19**	**.39**	**.31**	**.12**	.00	-.00	.00	.00	-.00	-.00	-.00	-.00	.00	.00	-.00
		p	1	.00	.00	.00	.00	1	1	1	1	1	1	1	1	1	1	1
	BDA-FSL2 fibers	r_p	-.02	**.24**	**.38**	**.34**	**.18**	-.00	-.02	.00	-.01	.04	-.06	.01	**.20**	.00	.00	.02
		p	.68	.00	.00	.00	.00	.94	.80	1	.79	.45	.14	.01	.00	1	1	.72
	BDA-DS somas	r_p	*.00*	*.07*	***.34***	***.24***	***.33***	***.37***	*-.00*	*.00*	*.00*	*-.00*	*.01*	*.07*	*.05*	*-.01*	*.00*	***.59***
		p	*1*	*.11*	*.00*	*.00*	*.00*	*.00*	*1*	*1*	*1*	*1*	*.89*	*.03*	*.09*	*.85*	*1*	*.00*
= 0.3mm	BDA-DS fibers	r_p	-.02	.02	**.33**	**.22**	**.43**	**.18**	-.02	-.04	-.02	-.04	-.04	**-.07**	**.23**	-.00	-.00	-.01
		p	.64	.67	.00	.00	.00	.00	.77	.35	.66	.44	.29	.04	.00	.94	1	.80
	BDA-FSL1 fibers	r_p	.00	**.20**	**.43**	**.40**	**.15**	.08	-.00	.00	-.01	-.00	-.00	-.00	-.00	.00	.00	-.00
		p	1	.00	.00	.00	.00	.19	1	1	.87	1	1	1	1	1	1	1
	BDA-FSL2 fibers	r_p	-.03	**.26**	**.43**	**.45**	**.20**	**.17**	-.03	.00	-.01	**.11**	-.06	.04	**.26**	.00	.00	-.03
		p	.58	.00	.00	.00	.00	.01	.67	1	.84	.02	.14	.28	.00	1	1	.55
	BDA-DS somas	r_p	*.00*	*.10*	***.34***	***.24***	***.31***	***.24***	*-.00*	*-.00*	*.00*	*-.02*	*-.00*	*.03*	***.10***	*-.01*	*.00*	***.41***
		p	*1*	*.04*	*.00*	*.00*	*.00*	*.00*	*1*	*1*	*1*	*.66*	*.95*	*.35*	*.00*	*.82*	*1*	*.00*
= 0.6 mm	BDA-DS fibers	r_p	**.09**	.02	**.36**	**.26**	**.41**	**.13**	-.04	-.03	-.02	-.03	-.05	-.07	**.23**	-.01	-.00	-.02
		p	.05	.69	.00	.00	.00	.04	.57	.56	.65	.47	.26	.04	.00	.91	1	.62
	BDA-FSL1 fibers	r_p	.00	**.22**	**.43**	**.44**	**.20**	**. 16**	-.01	.00	-.01	-.00	-.00	-.00	-.00	.00	.00	-.00
		p	1	.00	.00	.00	.00	.01	.88	1	.87	1	1	1	1	1	1	1
	BDA-FSL2 fibers	r_p	.01	**.26**	**.45**	**.48**	**.21**	**.22**	-.04	.00	-.01	**.10**	-.06	.05	**.23**	.00	.00	-.02
		p	.83	.00	.00	.00	.00	.00	.57	1	.80	.03	.14	.13	.00	1	1	.60
	BDA-DS somas	r_p	*.00*	*.08*	***.41***	***.29***	***.30***	***.32***	*-.00*	*-.00*	*.00*	*-.02*	*-.01*	*.05*	***.11***	*-.02*	*.00*	***.16***
		p	*1*	*.09*	*.00*	*.00*	*.00*	*.00*	*1*	*1*	*1*	*.61*	*.86*	*.15*	*.00*	*.74*	*1*	*.00*

3.3.5 Variability of inter-ROI connectivity correlations

Table 3.3-3 gives the Pearson's correlation (r) and Spearman's rank correlation (r_s and $(r_s)_{10}$) coefficients (mean value $\pm$ one standard deviation) with corresponding p values (mean value) of tractography-histology variables calculated from 30 DWI bootstrap samples. Figure 3.3-6 uses red markers to show the number pairs of bootstrap streamlines (mean and $\pm$ one standard deviation) and BDA-tagged fibers connecting to each one of the 17 projection regions for DS, FSL1 and FSL2 schemes with $d_w = 0$, 1 and 2 voxels. Each red line indicates the fitting line of these number pairs. The black markers and lines indicate the number pairs and regression lines calculated from the original dataset, which are also shown in Figure 3.3-3. Figure 3.3-7 illustrates the number of streamlines connecting to each one of the 17 projection regions based on both bootstrap samples and the original dataset for DS, FSL1 and FSL2 schemes with $d_w = 0$, 1 and 2 voxels. For the FSL1 and FSL2 cases in Figure 3.3-7, the number pair of bootstrap means vs. original number (indicated by red cross) for most of the projection regions fall close to the identity lines.

Table 3.3-3. Pearson's correlation, r, and Spearman's rank correlation, r_s and $(r_s)_{10}$, coefficients (mean value $\pm$ one standard deviation) with corresponding p values (mean value) of tractography-histology variables calculated from 30 DWI bootstrap samples. Significant correlations are shown in bold.

	$d_w = 0$mm	$d_w = 0.3$mm	$d_w = 0.6$mm
BDA fibers vs. DS streamlines	r **=0.83±0.02** $p < $ **0.0005**	r **=0.90±0.01** $p < $ **0.0001**	r **=0.92±0.005** $p < $ **0.0001**
	r_s =0.30±0.07 $p < $ 0.24	r_s =0.37±0.08 $p < $ 0.16	r_s =0.46±0.07 $p < $ 0.07
	$(r_s)_{10}$=0.61±0.10 $p < $ 0.21	$(r_s)_{10}$=0.65±0.12 $p < $ 0.15	$(r_s)_{10}$**=0.72±0.10** $p < $ **0.035**
BDA fibers vs. FSL1 streamlines	r =0.37±0.04 $p < $ 0.10	r **=0.76±0.07** $p < $ **0.0008**	r **= 0.92±0.04** $p < $ **0.0001**
	r_s =0.23±0.07 $p < $ 0.38	r_s =0.34±0.08 $p < $ 0.30	r_s =0.38±0.06 $p < $ 0.26
	$(r_s)_{10}$**=0.74±0.06** $p < $ **0.015**	$(r_s)_{10}$**=0.86±0.08** $p < $ **0.0014**	$(r_s)_{10}$**=0.88±0.06** $p < $ **0.0006**
BDA fibers vs. FSL2 streamlines	r **=0.43±0.03** $p < $ **0.03**	r **=0.79±0.06** $p < $ **0.0005**	r **=0.92±0.01** $p < $ **0.0001**
	r_s =0.26±0.03 $p < $ 0.34	r_s =0.38±0.03 $p < $ 0.17	r_s =0.40±0.04 $p < $ 0.15
	$(r_s)_{10}$=0.54±0.08 $p < $ 0.067	$(r_s)_{10}$**=0.66±0.05** $p < $ **0.044**	$(r_s)_{10}$**=0.77±0.05** $p < $ **0.044**
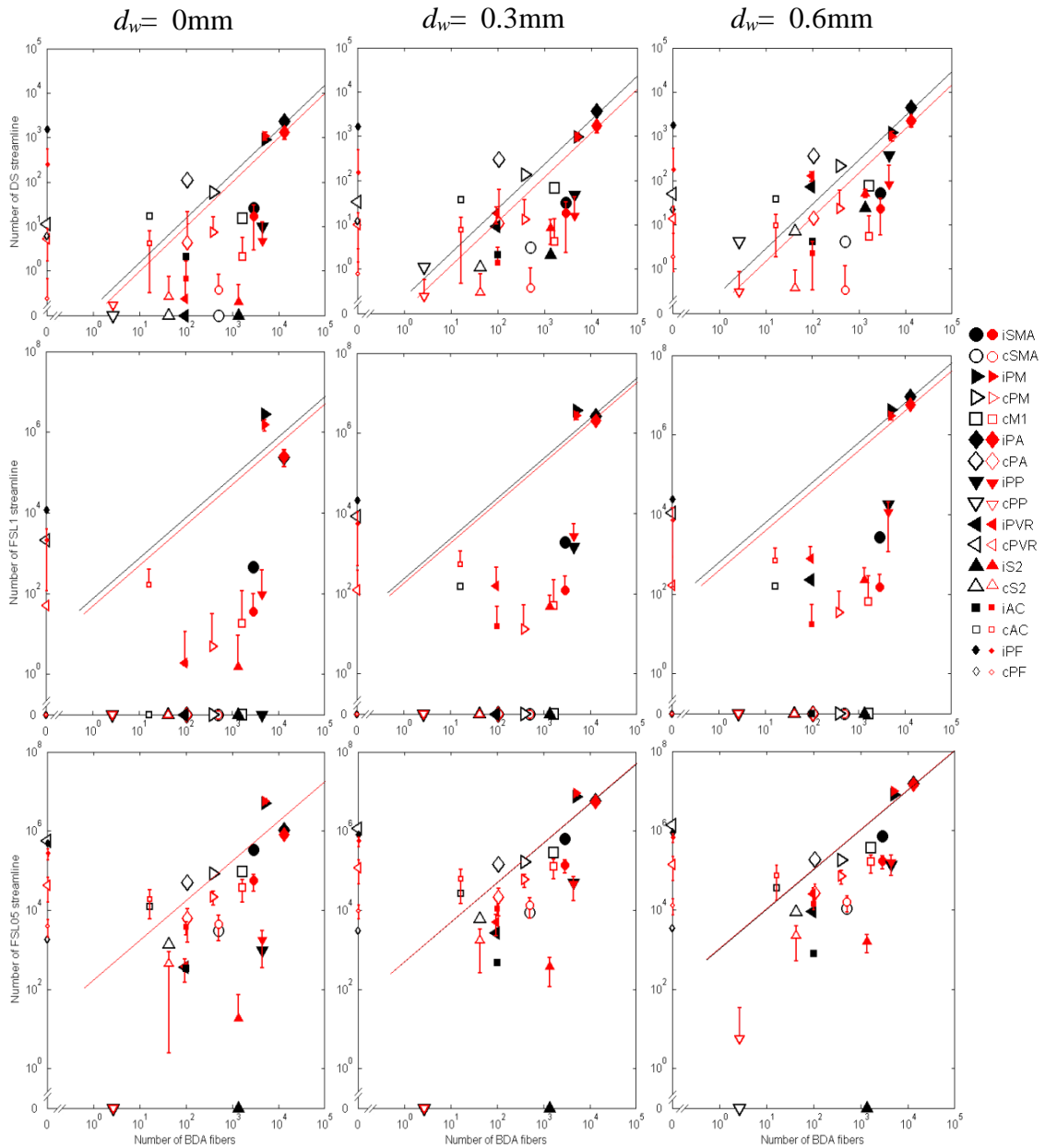
Figure 3.3-6. Bootstrap and original connectivity correlations between numbers of tractography-derived streamlines and numbers of BDA-tagged fibers across all the projection regions. The black markers in each plot indicate the original numbers pairs of tractography-BDA fibers connecting to the projection regions (as same as Figure 3.3-3). The black line in each plot indicates the least square fitting line calculated from the original number pairs. The red markers in each plot indicate the number of tractography-derived streamlines [mean (red marker) ±standard deviations (red error bar)] calculated from 30 bootstrap samples. Each red fitting line was calculated from the number pairs of the mean of bootstrap streamlines and BDA fibers.
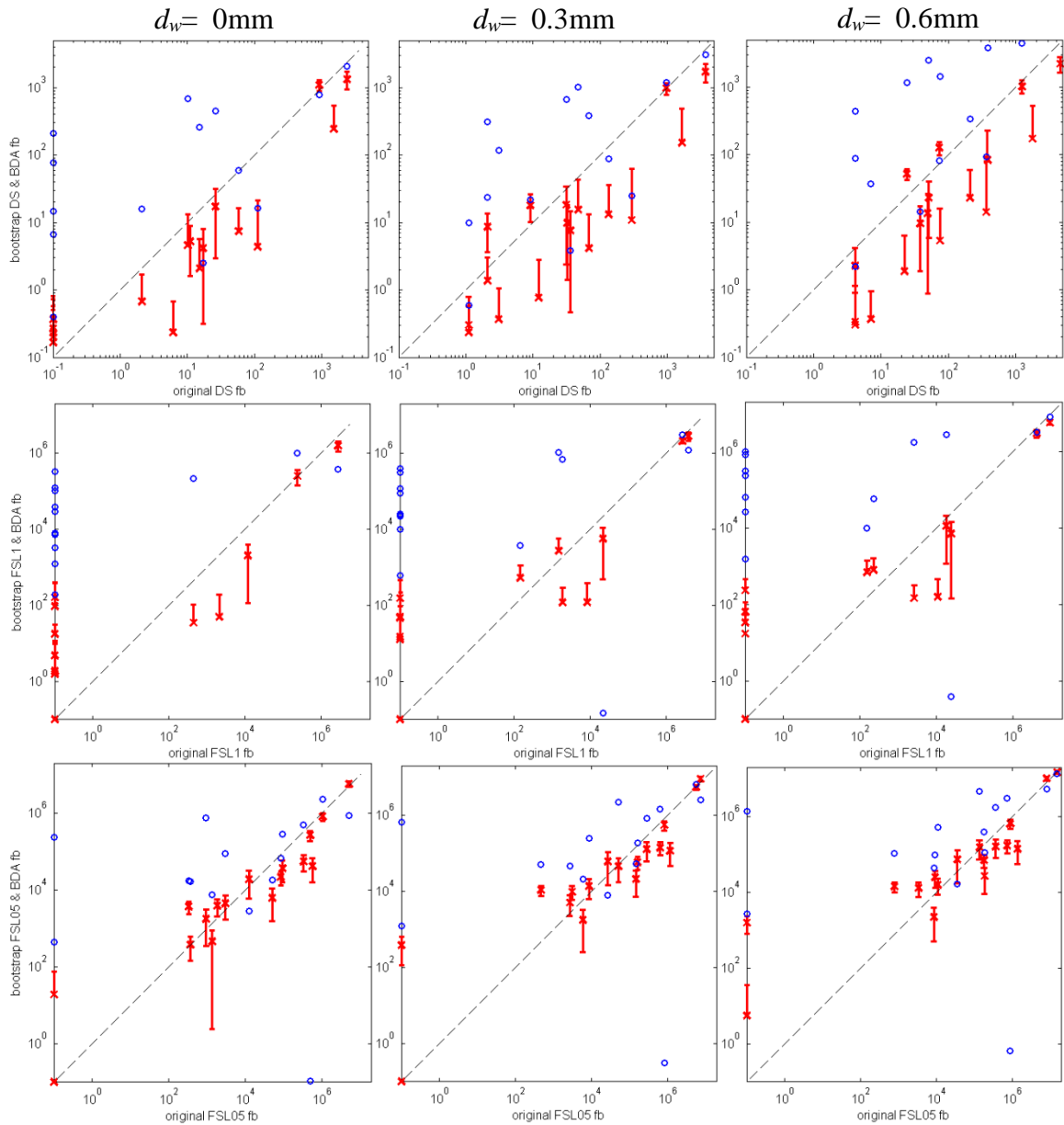
Figure 3.3-7. Mean (with standard deviation) number of bootstrap-derived streamlines and scaled number of BDA-tagged fibers connected to each individual target projection region vs number of original streamlines connected to the same target region. The dash line indicates the identity line. The red crosses and associated error bars respectively indicate the mean and standard deviation of the number of bootstrap-derived streamlines terminating in a specific projection region. The blue circle indicates the scaled number of BDA-tagged fibers (i.e., number of BDA fibers scaled such that the highest BDA count matches the highest tractography fiber count).

49

3.4 Discussion

In this study, we evaluated the correlation of histology- and tractography- derived connectivity between M1 and 17 other cortical regions. In each case, histology and tractography density maps were compared both between (Figures 3.3-2 and 3.3-3) and within (Table 3.3-2, Figure 3.3-4) regions. To the best of our knowledge, this is the first work to make direct comparisons of corticocortical connectivity derived from histology and DTI tractography.

Our results show that DTI tractography was capable of detecting all the cortical regions anatomically connected to M1 area (as in the DS scheme with d_w=0.6mm), but also produced false positive connections to other regions (all schemes). In addition, the correlation of inter- and intra- ROI connection strengths indicates that the tractography schemes we used do not have uniform sensitivity to anatomical connections, either across all ROIs or within a single ROI. Statistical analysis of Table 3.3-1 and visual inspection of Figure 3.3-2 support the conclusion that DTI tractography reliably identifies the regions with highest connectivity to M1. The Pearson correlation r ($p < 0.0001$) was highly significant for all schemes with $d_w = 0.6$mm in Table 3.3-1, however this measure emphasizes the strongest connections. When regions with weaker M1 connectivity are included in the Spearman correlation test, DTI tractography is not able to determine the rank order reliably (non-significant Spearman r_s for all schemes and seed depths). When the test is repeated with only the 10 regions most strongly connected to M1 included, the Spearman $(r_s)_{10}$ is highly significant. Hence, DTI tractography was not reliable in ranking the regions with weaker connectivity (i.e., number of BDA-labeled fibers smaller

than 100).

The two tractography algorithms used in the study were not compared in a rigorously equivalent manner. For example, the seed volume for DTIStudio was the entire brain whereas FSL was seeded only in the injection region. These seeding strategies were chosen to match the way the algorithms are generally used, in practice. Our aim was less to make a head-to-head comparison of the two methods and more to assess the accuracy of DTI tractography as usually practiced.

The standard deviations of the connectivity correlations based on bootstrap samples in Table 3.3-3 indicate that the variability of the correlations is increasingly small as d_w increases. However, comparison of the bootstrap-derived mean correlations in Table 3.3-3 with the original correlations in Table 3.3-1 reveals that the bootstrap-derived mean correlation coefficients were biased relative to the correlation coefficients computed from the original DWI data for some cases, especially for the DS cases. Moreover, from Figure 3.3-6 and Figure 3.3-7, we found that in the case of DS, most of the projection regions with strong histological connections to M1 have fewer bootstrap streamlines than the original streamlines and yet the decrease of bootstrap streamlines connecting to iPA cortex (the strongest histological connection to M1) increases the correlation coefficients. On the other hand, for FSL, the numbers of bootstrap streamlines connecting to the 17 projection regions do not have a significantly coherent change compared to the numbers of original streamlines, which keeps the bootstrap-based correlations consistent with original ones. Why then does the bootstrap for DS schemes decrease the number of streamlines? To find the answer, we listed the number of streamlines originating from the

51

IS and terminating in all target cortices, the average length of those streamlines, as well as the mean number of streamlines per voxel. These quantities were calculated from both original and bootstrap datasets for DS cases, as shown in Table 3.4-1. We found decreases in all three indices in DS bootstrap samples relative to the original (measured) data. The decreases occur mostly because the bootstrap-derived tensor orientations along the tracts were less coherent, as indicated by Figure 3.4-1AB, which implies that turning angles along the tract became larger so that streamlines stop faster than fibers calculated from the original data indicated by Figure 3.4-1CD. A possible underlying reason for greater noise in the bootstrap samples for DS cases is that the bootstraps overestimate the residuals, especially for the voxels with low FA, because the residuals also include the model errors from single-tensor estimation (see Figure 3.4-2).

Table 3.4-1. Number of selected streamlines, average length of selected streamlines and mean number of streamlines per voxel calculated from originally acquired DWI data and residual bootstrap DWI samples.

		Number of Streamlines		Average Length of Streamlines (mm)		Mean Number of Streamlines/Voxel	
		Original	*Bootstrap*	*Original*	*Bootstrap*	*Original*	*Bootstrap*
DS	$d_w=0$	7587	5262±92	14.6	8.2±0.2	15.9	9.6±0.4
	$d_w=1$	9516	6379±132	17.6	9.2±0.3	18.2	10.5±0.4
	$d_w=2$	11219	7532±154	19.0	9.9±0.4	19.0	11.0±0.4
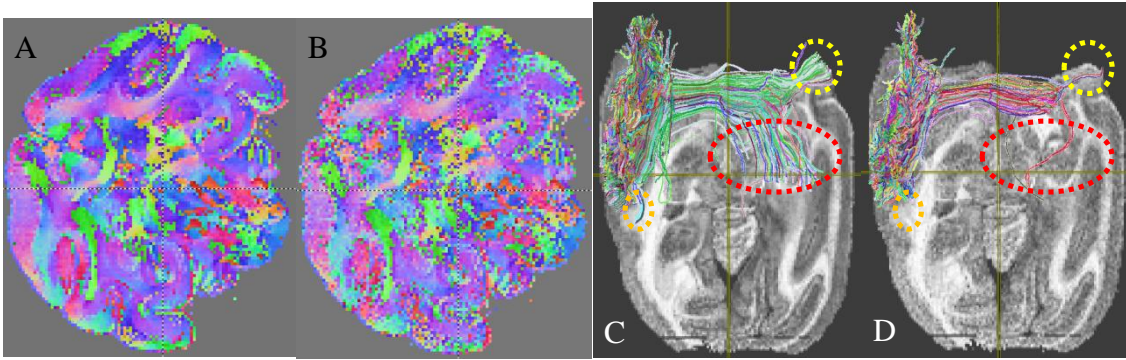
Figure 3.4-1. Color-coded maps of the primary eigenvector and DS streamlines calculated from the original DWI dataset and one bootstrap sample dataset. The color-coded map of primary eigenvectors (A) based on original DWI dataset shows smoother change of color than the color-coded map (B) based on the bootstrap dataset. The selected fibers (C) calculated from the original DWI dataset are greater in number and length than the fibers (D) calculated from bootstrap dataset. This relation is clearly observed in the red, yellow and orange circles.
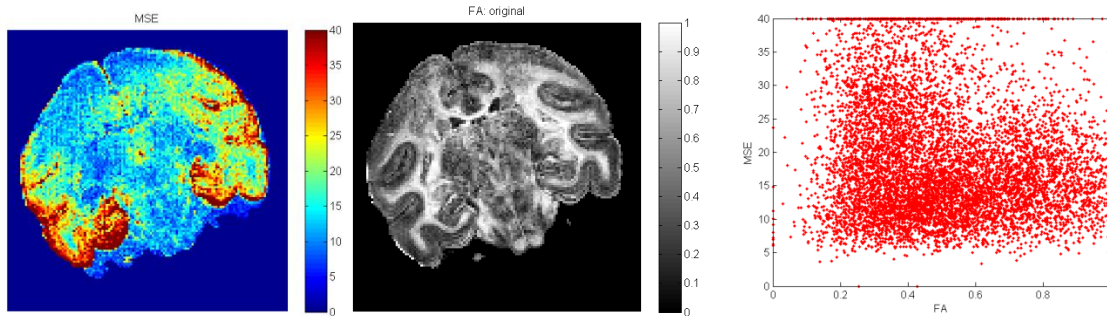
Figure 3.4-2. Mean square error (MSE), FA scalar map and MSE vs. FA plot for the same coronal slice extracted from one bootstrap sample dataset.

The proportional relationship between the BDA-labeled somas and BDA-labeled fibers across all the ROIs was significant in our study, due to the reciprocal nature (i.e., the number of afferent nerve fibers is comparable to the number of efferent nerve fibers) of motor cortex cortical connections. However, other networks may not have reciprocal connections, and therefore the utility of BDA-labeled somas in validation studies is

probably limited.

The tracer BDA was used in this study because it is transported in both anterograde and retrograde directions, labeling both afferent and efferent projections of the injected cortical region, which is analogous to the propagation of DTI streamlines from the seed region. Moreover, since BDA (in contrast to WGA-HRP [79]) does not diffuse much in brain tissue, the injected tracer was confined to the forearm M1 representation area. Most importantly, BDA provides highly sensitive and exquisitely detailed Golgi-like labeling of somas, axons and terminals [62], which better facilitates quantitative analysis of individual fibers than WGA-HRP does.

There are several limitations to the study. First, only connections to the forearm region of M1 were quantified—measurements of the accuracy of DTI connectivity to this region may not generalize to other areas in M1 or to other cortical networks. Second, BDA was injected at approximately 1mm intervals covering the forearm region (Figure 3.2-1). This interval was chosen because the tracer spreads in the tissue about 0.5mm from the needle location and the goal was to tag all axons in the region. However, it is possible that uptake of the tracer was not uniform over the forearm area while the distribution of tractography seed points was uniform. Hence, it is possible that the BDA and seed point distributions were not identical in the injection region, which could bias the results toward those locations within the region where BDA uptake was higher. In addition, in the radial direction, the BDA injection was not strictly confined to gray matter, but extended slightly into the white matter immediately underneath the cortex, which means that fibers of passage underneath the injected cortex may have taken up

BDA as well. Seed regions that extended one or two voxels ($d_w = 0.3$ and 0.6mm) into the subcortical white matter helped to match the injection volume. Third, imperfect micrograph-to-DTI spatial registration may introduce bias in DDMs. Although the overall error in our registration procedure was likely on the order of 1 voxel (=0.3mm) [74], the local error close to the GWM-interface was more difficult to control and estimate because there were fewer apparent features to be captured as landmarks. Fourth, the MRI acquisition had limited SNR (~30) and number of diffusion directions (n=31), which likely affected sensitivity to small fiber components. However, these are typical parameters for many DTI experiments, including *in vivo* human studies. Finally, this study used two approaches to tractography (deterministic and probabilistic), implemented in two of the most commonly used analysis packages (DTIStudio and FSL). However, the results may not apply to other algorithms. The framework for comparison to histology used in this study could be applied to other algorithms.

Probabilistic tractography schemes were expected to provide stronger correlations than deterministic tractography due to higher sensitivity to the non-dominant pathways where fibers cross. However, our results show no significant difference in correlations between these methods. This might be due to the limitations of our DWI acquisition, since 32 diffusion directions only allow FSL to resolve crossing angles more than 60° within a voxel [26]. Additionally, due to partial volume averaging, the termination mask used in FSL tended to stop some streamlines which otherwise would travel along the WGM interface and then stop at locations father away from seed mask. This phenomenon is shown as a 'hot color' ring surrounding the injection region in the Fig. 3.3-5D and E.

The results of this study show that connectivity measured by DTI tractography is

strongly correlated with anatomical connectivity when measured on the scale of major cortical regions (Figure 3.3-3). At a finer scale (i.e., within regions), the DTI DDMs are somewhat less reliable (Table 3.3-2). This implies that as cortical parcels are subdivided to achieve higher resolution in connectivity maps, the reliability of those maps may decrease dramatically, due to inaccuracies in streamline terminal location. Our results suggest that interference from strongly anisotropic bundles that cross pathways of interest tends to bias DTI connectivity measurements. Such bias would likely be consistent across repeated scans and across individuals, if the fiber geometry was consistent. Hence, reproducibility of DTI connectivity measurements is not, in and of itself, an indication of reliability. More accurate connectivity measurements will rely on detection of fibers that comprise a small minority of the total fiber population within a voxel. This may be possible with High Angular Resolution Diffusion Imaging (HARDI) methods, although the sensitivity of HARDI to small fiber populations has not been studied extensively. Improvements in modeling fiber orientation distributions and tracking fibers of interest through ambiguous crossing regions will be critical to increasing the accuracy of diffusion MRI measurements of cortical connectivity.

Finally, the squirrel monkey replicates much of the macroscopic structure of the human nervous system, yet it is possible that the human brain has more complex microstructure. Thus we need to be cautious when interpreting the accuracy of DTI measurements in human brain data given only the monkey's validation results.

3.5 Conclusion

DTI tractography is capable of providing true positive connectivity for most or all cortical regions with anatomical connections to M1 in the squirrel monkey, but may also produce false positive connections. Deterministic tractography can provide inter-regional connectivity measures as accurate as probabilistic tractography under some situations. However, DTI tractography is not uniformly sensitive to connection strength either across or within connecting to regions.

CHAPTER IV

CAUSES OF DISAGREEMENT BETWEEN DTI TRACTOGRAPHY AND

MICROSCOPY

4.1 Introduction

Diffusion tensor imaging (DTI) is a popular tool for non-invasive assessment of structural connectivity of the human brain. However, the accuracy of connectivity measurements based on DTI techniques has not been thoroughly investigated. In chapter III, the corticocortical connectivity measured by DTI tractography was compared to the connectivity traced by traditional histology methods – the current 'gold standard'. Although a basic level of agreement was found in our study, disagreements with the true connectivity were expected and found for both deterministic and probabilistic methods. To further understand and interpret these results, we did experiments to reveal the correspondence between DTI tractography-derived white matter pathways and the anatomical pathways, since it is the white matter that connects one cortical area to another. The deviations were localized by comparing the two sets of pathways. Potential causes of the deviations were investigated by comparing the primary direction of the tensor to the high resolution anatomical fibers within the same 'error' voxel. The key step to extend 2D analysis on anatomical data to 3D is to obtain 3D histological fiber orientation distribution (hFOD) data, thus we obtained z-stack micrographs of anatomical

sections and developed a framework to extract 3D hFOD information.

4.2 Methods

The original anatomical tissue sections and diffusion-weighted images were the same data acquired in part 3.2.1. The multi-step registration process from standard micrograph space (0.5X) to the DTI space was described in part 3.2.2 and the stored deformation file was used to transfer data from one space to another.

4.2.1 Overlaying anatomical white matter pathways in DTI space

To find voxels where the DTI streamlines deviate from anatomical pathways, we need to compare DTI and anatomical pathways in the same space. For this reason, we reconstructed the BDA-labeled fiber pathways in DTI space and overlaid the DTI streamline pathways on the BDA-labeled pathways, which are described below.

To obtain BDA-labeled fiber pathways, 1.25X (the minimum magnification required to distinguish two adjacent BDA fibers) panoramic micrographs covering the entire tissue section were acquired for all the BDA-visible sections. Each component micrograph was taken by a Nikon DS-Ri1 color camera mounted on a Nikon AZ100M widefield microscope. The commercial software Adobe Photoshop CS3 (San Jose, CA) was used to merge the component photographs into a panoramic micrograph. Then we registered each 1.25X panoramic photo to its corresponding microphotograph in 'standard micrograph space' (0.5X, see more detail in part 3.2.1).

Because BDA-labeled fibers and grey matter did not present enough distinct features

for the fiber segmentation algorithm to detect, the whole white matter area in each registered micrograph was manually extracted first, to prevent the fiber segmentation algorithm from failing to distinguish BDA-labeled fibers from grey matter. Then, all the fibers were segmented by a series of morphological processes. We then divided each micrograph into 256×256 square grids, calculated the number of fiber-occupied-voxels in each square and generated 'fiber volume maps' whose voxel values represented the fiber occupied volume fraction within that voxel. Spatial transformation and compensation were calculated as in part 3.2.2. The final step was to extract isosurfaces from volume maps and reconstruct the tubular surface delineating the BDA-labeled fiber pathways.

We used the same scheme to obtain deterministic and probabilistic tractography results as described in part 3.2.2. For the 'DS' scheme, continuous 3D coordinates of fibers produced by DTIStudio were used to reconstruct explicit fiber pathways. The fiber density of each voxel was defined by the number of fibers passing through or ending within that voxel. For 'FSL' (i.e., FSL1 and FSL2) schemes, we obtained the 3D fiber density map instead of the explicit fiber pathways, which is the direct output of FSL tool 'probtrackx'. Then we reconstructed isosurfaces of the density maps to help visualizing the fiber-occupied pathways.

To indicate the general agreement between DTI tractography-derived and anatomical white matter pathway, we calculated the agreement coefficient (AC) given by,

$$AC = \frac{2(V_B \cap V_D)}{V_B + V_D}, \tag{4.2-1}$$

where V_B (or V_D) is the density-weighted BDA (or DTI) volume. The densities were the normalized fiber densities calculated from 'DS' scheme or 'FSL' schemes. This density-

weighted agreement coefficient provides a more realistic estimate of agreement than a simple measurement of volume overlap [51].

For deterministic streamlines, we were able to determine the spatial coordinates for each streamline; thus we could localize the 'error' voxel by judging whether the coordinates along an individual fiber lie outside the BDA-labeled fiber pathways. For probabilistic streamlines, we only had density maps from FSL instead of fiber coordinates, so we needed to find the 'error' voxel by searching the voxels outside the BDA fiber pathways that had significant FSL density values.

4.2.2 Overlaying DTI output in high resolution microscopy space

To visualize more details than just isosurfaces of the DTI-derived and anatomical fiber pathways, we transferred DTI related information to the high resolution microscopy space and compared them with the anatomical information in the microscopy space.

The continuous coordinates of the fibers calculated by DTIStudio were transferred to standard micrograph space using the stored inverse deformation files computed by our multi-step registration process. A 3D fiber segment was assigned to a certain 2D anatomical micrograph if the fiber segment was closest to this section.

DTI tensors were fitted by DTIStudio and the locations of the tensors were transferred to block face space and then to the standard micrograph space also using the inverse deformation files computed before. Additionally, the orientations of the tensors in micrograph space were recalculated using the Preservation of Principal Direction (PPD) [80] method. Finally, the isosurfaces of those reoriented tensors were rendered and

overlaid on the high resolution micrograph.

4.2.3 Analysis of crossing fibers in 'error' voxels

DTI is sensitive to all fibers lying in a voxel while BDA only labeled the fibers connecting to M1, which means BDA labeled fibers in one voxel might be the subset of the DTI-detected fibers. Therefore, we chose a non-selective labeling method, i.e., a myelin stain, to tag all the anatomical fibers for the purpose of white matter comparison.

Confocal microscopy was used to provide 3D histological information by scanning the confocal plane from bottom to top of the myelin-stained section (z-direction) and then capturing micrographs of different fields of view in the confocal planes (x-y plane). Three dimensional histological fiber orientation distribution (hFOD) functions for each DTI voxel were exacted from the z-stacks as follows.

Two optional methods were tried in order to obtain more accurate hFODs. The preprocessing steps (i.e., denoising, intensity normalization, deconvolution [81], segmentation and spur removal) for those two methods were the same. One method included the following steps: 1) repeatedly thinning the segmented fibers until the fiber skeletons were obtained; 2) detecting all the crossing points of the skeletons; 3) for skeletons without any crossing points, extracting the coordinates of the center of all the skeleton voxels for each fiber and then fitting those coordinates to a smooth curve; 4) for the skeleton with crossing point(s), dividing this skeleton into sub-skeletons using the crossing point as the cutoff point, and then fitting each sub-skeleton into a curve as in step 3); 5) estimating the 3D angle for each fitted curve and then adding up the number of voxels in fiber segments of the same orientation—this is interpreted as the value of the

distribution at that orientation and voxel (we should notice that the calculated 3D angles are continuous variables with some uncertainty, so we divided the azimuthal angle range of $360\,°$ into 36 bins and the polar angle range of $180\,°$ into 36 bins to hold the orientations); 6) plotting the discrete hFOD.

The other optional method employed a 3D extension of the 2D Fourier directional filtering method [82, 83] and included the following steps: 1) converting the segmented data to the frequency domain by performing 3D Fourier transformation; 2) in the frequency domain, employing, respectively, a set of 3D directional filters with different angular orientations uniformly distributed on the unit sphere; 3) performing inverse Fourier transformation to each filtered image and summing up the number of voxels above the assigned threshold; 4) plotting the hFOD.

To compare the diffusion tensor to the hFOD in the same space, the tensor corresponding to each position in the micrograph space was calculated using partial volume interpolation of the original DW images. In order to preserve the tensor orientation in the micrograph space after registration, the tensor was rotated using the preservation of principal directions reorientation strategy [80].

4.3 Results

4.3.1 Correspondence of white matter pathways in DTI space

Figure 4.3-1 displays the volume of BDA-labeled fibers overlaid respectively on the DS fibers (first row of figure 4.3-1) and the volume occupied by FSL fibers (last two rows of

figure 4.3-1) with $d_w = 0$mm, 0.3mm and 0.6mm, rendered within the external surface of the grey matter (glassy blue surface) to provide an anatomical reference. The superimposition of BDA pathways and tractography-derived pathways provides a visual overview of the correspondence of the two pathways in white matter. False negative results of DTI measurements are those voxels occupied only by BDA-labeled fibers (red color in figure 4.3-1), e.g., the red voxels in the left internal capsule pointed to by black solid arrows in the first column and those voxels in the left posterior part of anterior parietal lobe pointed to by black solid arrows in the second column. False positive results are those voxels only occupied by DTI-tractography fibers (blue lines in the first row and green volume in the last two rows), e.g., the voxels in the right premotor area pointed to by empty black arrows.
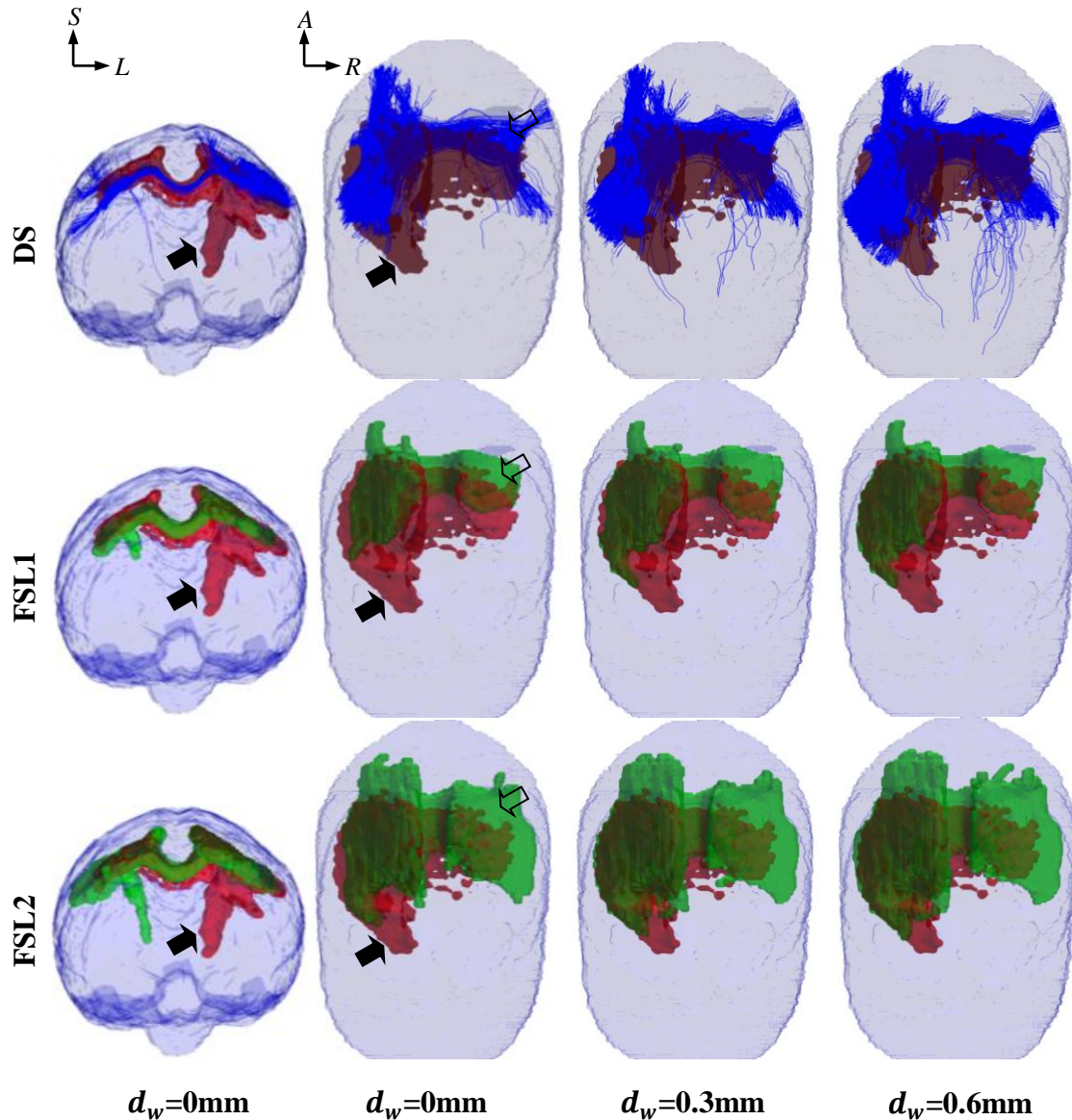
Figure 4.3-1. Frontal and dorsal view of the volume occupied by BDA-labeled fibers (red volume) overlaid on the 'DS' fibers (blue lines in first row) and 'FSL' fiber-occupied volumes (green volume in last two rows) with d_w = 0mm, 0.3mm and 0.6mm (corresponding to the first two columns, the third column and the fourth column), rendered within the external surface of grey matter (outermost transparent blue surface). Some false negative and false positive voxels are highlighted by the solid and empty black arrows, respectively.

Table 4.3-1 shows the density-weighted agreement coefficient, AC, for each tractography scheme using seed region with different d_w. For all three tractography schemes, as d_w increases, the agreement coefficients increase. The two FSL schemes (i.e., FSL1 and FSL2 schemes) have higher agreement coefficients than the DS scheme for each d_w.

Table 4.3-1. Density-weighted agreement coefficients (AC) of three specified tractography schemes (in rows) using seed regions with three depths into white matter, d_w (in columns).

	d_w		
	0mm	0.3mm	0.6mm
DS	0.55	0.62	0.67
FSL1	0.62	0.68	0.71
FSL2	0.71	0.78	0.81

4.3.2 Overlay white matter pathways in micrograph space

Figure 4.3-2 shows DTI-tractography-derived pathways (blue streamlines) superimposed on five BDA-labeled sections (0.5X, 256×256 pixels). Adjacent BDA sections are separated by 3mm in the intact brain. In section s174, there were only a few BDA-labeled fibers extending along the anterior-posterior direction to or from the left SMA, but the DTI streamlines also propagated to lower white matter of the left hemisphere and the right hemisphere as well as the left SMA. In section s234, the BDA-labeled fibers went up to the left SMA and ran to the right hemisphere along the corpus callosum (CC), while DTI fibers didn't go to the left SMA and propagated much farther in the right hemisphere than the BDA fibers. In the section 294, DTI fibers didn't cover the BDA fibers

propagating along corpus callosum. In the section 354, DTI fibers covered less than the BDA fibers in the left hemisphere. In the section 414, the BDA fibers covered the bottom 2/3 part of left parietal lobe, but the DTI fibers only covered the bottom 1/3 part.
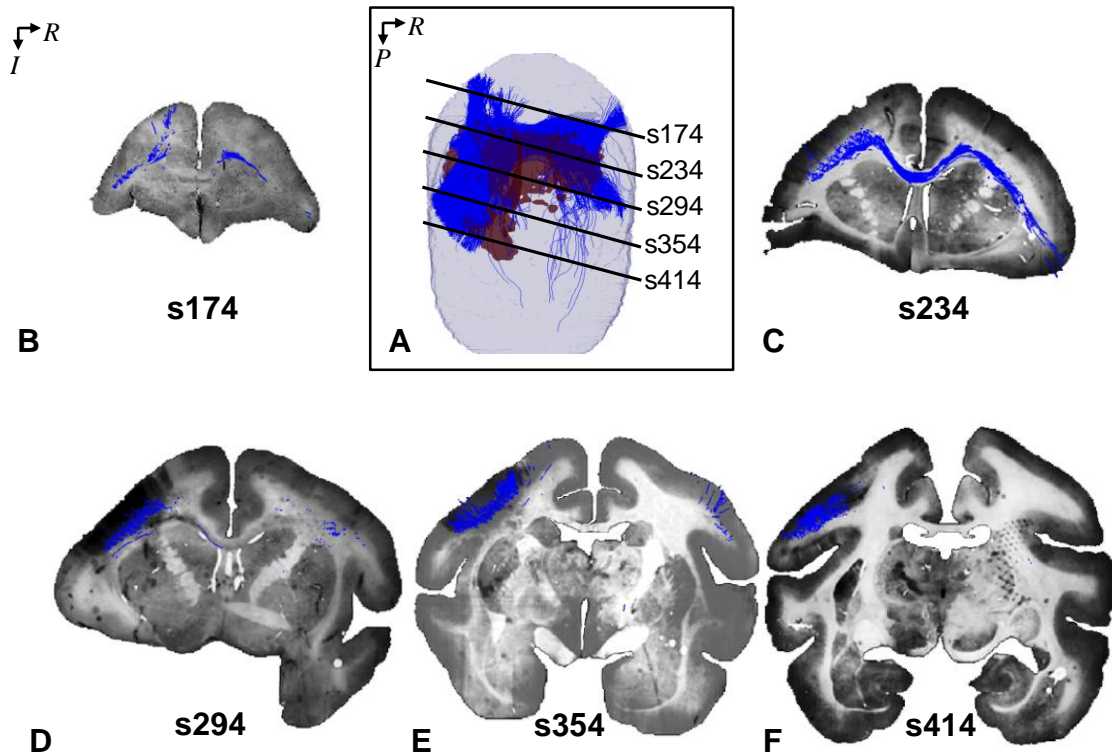
Figure 4.3-2. DTI fibers overlaid on five BDA-labeled sections. (A) shows the positions of five sections depicted by the straight black lines in 3D volume. The blue streamlines represent the fibers calculated from 'DS' scheme and the red surface encloses the BDA-labeled fiber volume. (B-F) show the DTI fibers overlaid on five selected BDA-labeled sections.

Section 294 was analyzed at higher resolution to display 3D diffusion isosurfaces overlaid on the high resolution BDA-labeled fibers, shown in figure 4.3-3. Although BDA-labeled fibers connecting the injection region to the contralateral hemisphere run along the left-right direction through the corpus callosum in the plane of figure 4.3-3A,

the principal diffusion direction (corresponding to the direction of most fibers in these voxels) estimated from DWI data is oriented along the anterior-posterior direction just under the injection region (indicated by the green color of diffusion isosurfaces at the foreground of Figure 4.3-3C) and superior-inferior direction in deeper white matter (indicated by the blue color of diffusion isosurfaces in the foreground of Figure 4.3-3D). The disagreement between the BDA fibers bound for the contralateral hemisphere and the dominant fiber orientation estimated from DWI data prevents most DTI streamlines from reaching the midline and the other hemisphere. In fact, the strong anterior-posterior orientation of tensors immediately under the injection region is partially responsible for the strong (false positive) connectivity to the ipsilateral prefrontal cortex (Figure 3.3-4 in the previous chapter) measured with both the DS and FSL2 schemes.
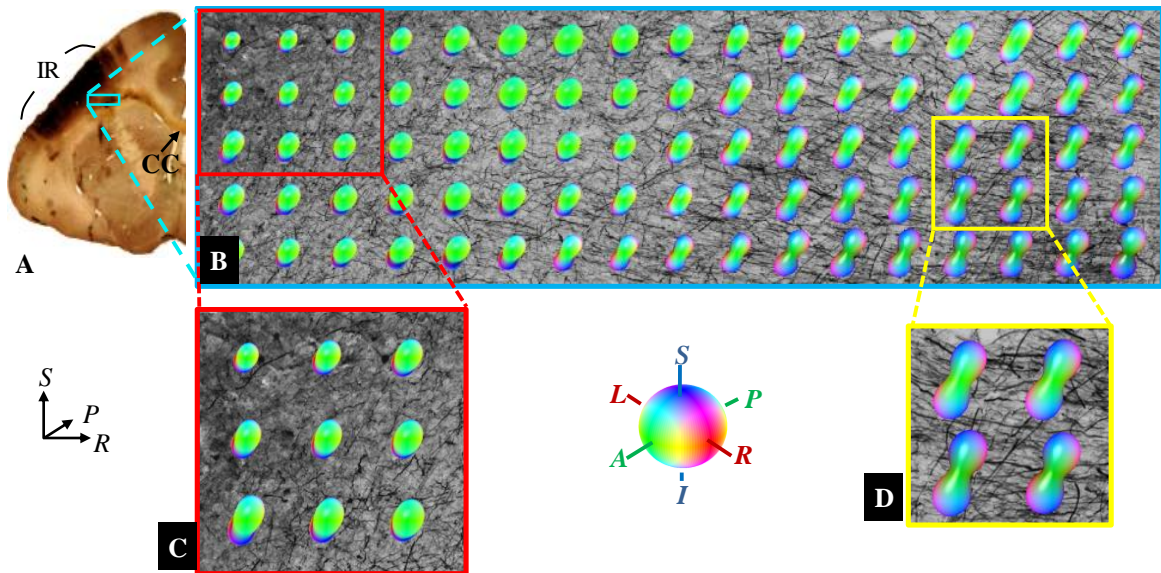
Figure 4.3-3. 3D diffusion isosurfaces overlaid on BDA-labeled fibers in crossing fiber regions in the high resolution micrograph space. (A) shows the left hemisphere of the BDA-labeled section 294 (0.5X). The background of (B) is the high resolution BDA micrograph (4X) of the white matter under the injection/seed region. Diffusion isosurfaces calculated from the tensors are color-coded according to anatomical orientation and scaled in size by the local fractional anisotropy. (C) and (D) show details immediately under the injection region (IR) and in deeper white matter, respectively.

Probabilistic tracking methods based on the multi-tensor model are predicted to be better able to resolve crossing fibers. However, the histology versus FSL fiber correlations shown in Table 3.3-1 are not significantly higher than the histology versus DS fiber correlations in this study. Figure 4.3-4AB shows that FSL2 scheme was also limited by partial volume averaging in our dataset. The FSL2 streamlines did not reach the WGM interface (indicated by the translucent white contour) under the contralateral PM cortex. Figure 4.3-4C displays the two fiber orientations (indicated by the short blue line and red line) estimated by the FSL2 scheme in each white matter voxel immediately

underneath the contralateral PM cortex. The vast majority of axons in these voxels travel parallel to the WGM interface and strongly bias the FSL-estimated fiber orientations also to be nearly parallel to the WGM interface. All six FSL cases (two ARD values, three seed region depths) were subject to similar limitations (although it is possible that the estimated orientations could be more accurate at higher SNR and/or b-value [26]). In summary, partial volume averaging of diffusion tensor data is likely a major source of error in our cortical connectivity measurements for both deterministic and probabilistic tracking algorithms.
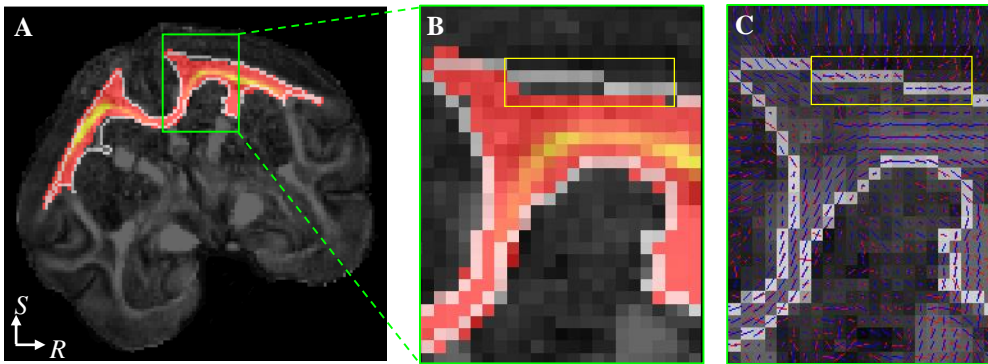
Figure 4.3-4. FSL2 (d_w=0.6mm) outputs overlaid on a fractional anisotropy (FA) map in DTI space. (A) Coronal slice showing the FSL2 output density map, i.e., yellow-red color map, superimposed on a grayscale FA map. The white contour labels the WMG interface. (B) and (C) show an enlarged region of interest in the superior part of the contralateral hemisphere. Blue and red lines in (C) represent dominant fiber orientations, estimated by the FSL bedpost tool.

Because BDA only stained fibers originating from the left M1 cortex while myelin stained all the axons existing in the tissue, high resolution micrographs of BDA-labeled fibers and myelin-stained fibers within the same area were compared. Figure 4.3-5 illustrates an example of 2D BDA-labeled fibers, myelin-stained fibers and 3D DS

diffusion isosurface within the same voxel (0.3mm×0.3mm) located in the left hemisphere about 2mm directly under the premotor (PM) cortex. The BDA reveals two major fibers bundles which run from superior to inferior and from left to right, shown in figure 4.3-5B. It appears that the bundle propagating from left to right is denser in axons than the other. Figure 4.3-5C shows two major bundles running along the same directions as the BDA fibers, but the major bundle is the one running from top to bottom, which is the same direction as indicated by the shape of diffusion isosurface in figure 4.3-5D.

| BDA (0.5X) | BDA (4X) | Myelin (4X) | Tensor |
| (A) | (B) | (C) | (D) |
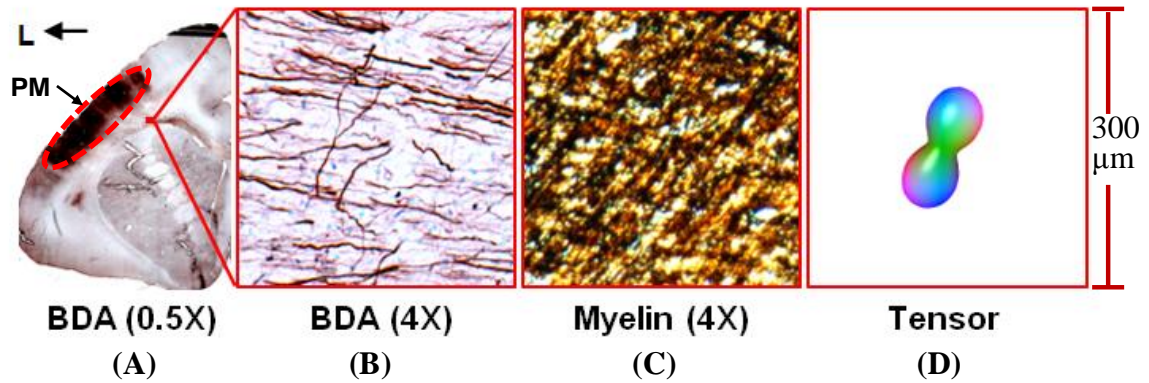
Figure 4.3-5. An example of (B) BDA-labeled fibers (4X), (C) myelin-stained fibers (4X) and (D) the diffusion isosurface within the same 0.3mm×0.3mm voxel located in (A) the left hemisphere of a BDA-labeled section (0.5X) far under the premotor (PM) cortex (A).

4.3.3 Z-stack analysis framework

Figure 4.3-6 displays the results of extracting an hFOD from a simulated z-stack. The simulated fiber bundles have two directions ([1 1 0] and [-1 -1 -1]) with equal fraction (0.5 for each bundle), as shown in figure 4.3-6A. The diameter of each cylinder bundle is 2μm, which is comparable to the actual size of BDA-labeled fibers. The FOV, 300μm×300μm×20μm, of the simulated data is chosen to be comparable to the actual

71

BDA section (i.e., the thickness of the shrunken BDA section is about 20μm) and the real DTI voxel size (i.e., 300μm×300μm). After applying the skeletonization algorithm, the 3D skeleton voxels of each fiber bundle are shown by the yellow sticks in figure 4.3-6B, and then fitted by connecting straight red lines centered on the skeleton. The FOD in figure 4.3-6C was obtained from the angles and number of voxels in those fitted lines. The color and peak orientation of each FOD lobe represent the orientation of the fiber bundle, and the length of the lobe represents the relative number of fibers propagating along that direction. Figure 4.3-6D shows the 3D filter (yellow shadow) overlaid on the Fourier transformation of the simulated data. The FOD in figure 4.3-6E was rendered using a spherical harmonic algorithm [84].

Figure 4.3-7 illustrates an example of a real Z-stack of BDA-labeled fibers imaged in differential interference contrast (DIC) mode. Three planes are located in the top (A), middle (B) and bottom (C) of the stack which has 44 planes in total. The fiber segment pointed to by the black arrows appears more and more apparent, and the fiber branch pointed to by red arrows gradually disappears from the top to bottom, which indicates the through-plane information of the BDA-labeled fibers can be captured in DIC z-stack micrographs.
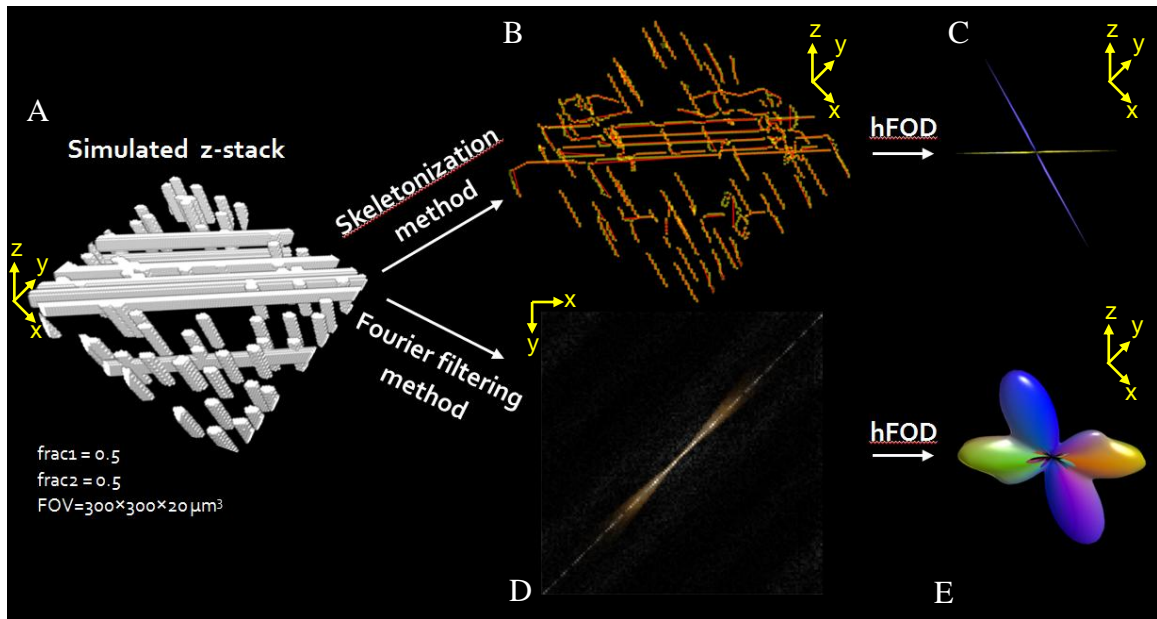
Figure 4.3-6. An example of extracting histological fiber orientation distributions (hFODs) from a simulated Z-stack using the skeletonization and Fourier filtering methods. The original simulated crossing fiber bundles (A) with two orientations and equal fractions. The skeleton voxels of the bundles and the fitting lines of the skeleton are shown by yellow volume and red lines in (B). The Fourier transformation of the original data in (D) was overlaid by an orientation filter represented by the yellow shadow. The FODs obtained from the two different methods were rendered directly (C) and using a spherical harmonic fitting algorithm (E).
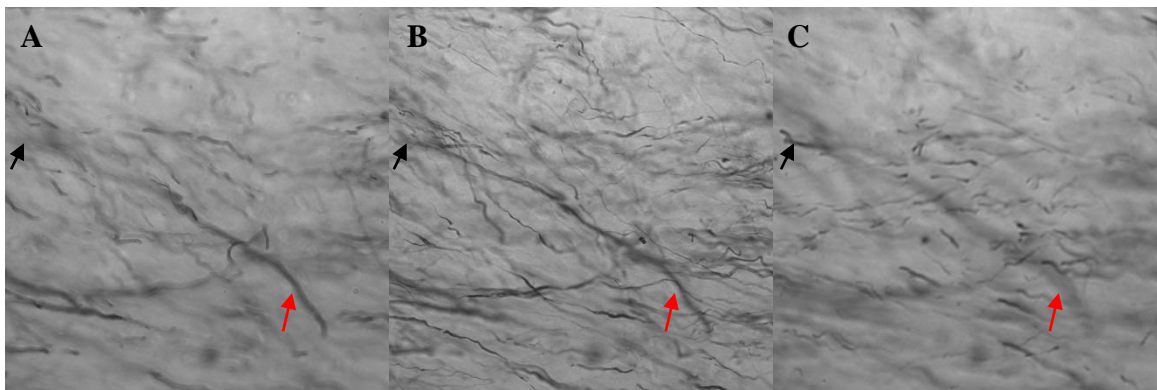
Figure 4.3-7. An example of a real Z-stack of micrographs showing BDA-labeled fibers in differential interference contrast (DIC) mode. Three planes located in the top (A), middle (B) and bottom (C) of the whole stack are selected to show the gradual change of the fibers which carries z-direction information on orientation. The black and red arrows point to the examples of fiber braches changing significantly from the top to bottom plane.

The FODs calculated from the real Z-stack of BDA-labeled fibers using the two (skeletonization and Fourier) methods are shown in figure 4.3-8. Both results are rendered using spherical harmonic representations. The major FOD lobe from figure 4.3-8A points approximately 30 degrees (counterclockwise) from the horizontal direction while the major FOD lobe from figure 4.3-8B points about 20 degrees up from the horizontal direction.

Figure 4.3-8. An example of the extracted hFODs using the skeletonization (A) and Fourier filtering (B) methods, overlaid on one plane of the real Z-stack micrographs.

4.4 Discussion

Several comparison examples in this chapter demonstrate that crossing fibers and the partial volume effect might lead to inaccurate or incomplete fiber tracking results even when the multi-tensor model is used to estimate multiple fiber orientations in one voxel. They also demons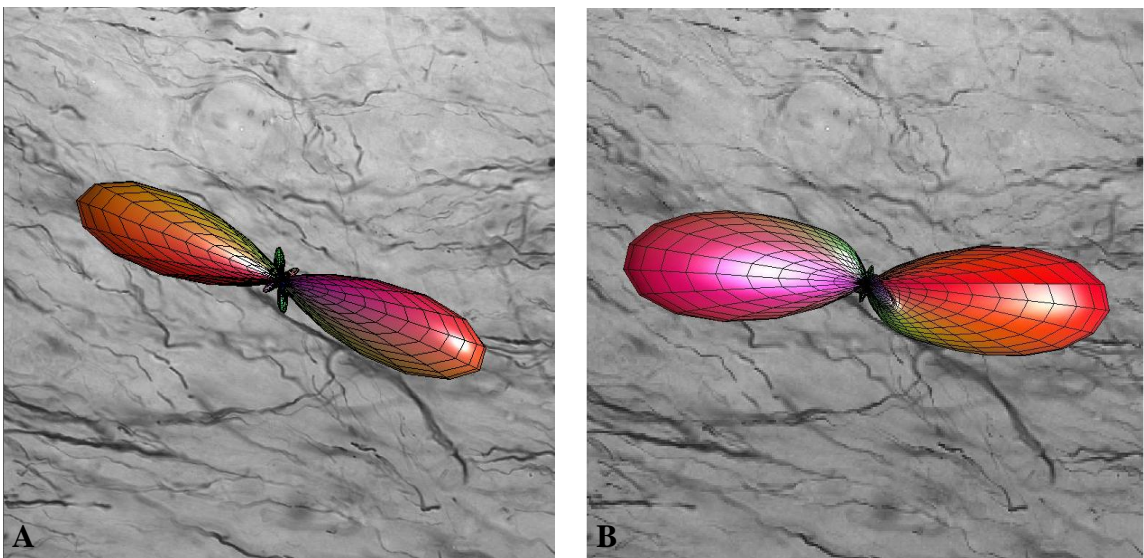trate that these factors might significantly bias the fiber tracking results, particularly if they occur close to the seed points. Although the quantitative comparisons between DTI tractography-derived and histological fibers connecting to M1 in Chapter III could not be generalized to other cortical networks, the reasons for the disagreement shown in this chapter could be applicable to all fiber bundles which run into crossing fibers or partial volume effects.

Each of the two methods we used to analyze micrograph z-stacks is limited in a different way. For the skeletonization method, there are two key steps that determine the quality of the result: 3D segmentation and skeletonization. We used the free skeletonize-3D plugin (http://fiji.sc/wiki/index.php/Skeletonize3D) [85] in the FIJI package (http://fiji.sc/ wiki/index.php/Fiji) to find the centerline of each fiber (or segment) in our study; however, the skeletonization result depends critically on the segmentation result due to its sensitivity to noise spurs in the real data. If the spurs cannot be removed effectively, they will form a 'false branch' of the centerline, which will bias the analysis of the orientation distribution. Additionally, the skeletonization method could be only used to analyze those micrograph data in which the individual fiber objects could be segmented. Accordingly, myelin-stained data in our study could not be analyzed by this method. For the Fourier filtering method, segmenting individual fiber objects is not

necessary, but a set of directional filters need to be used in Fourier domain to filter out fibers distributed along other directions. The accuracy of the resulting orientation distribution depends on the spread angle of each cone-shaped filter. Therefore, in the future work, the accuracy and noise sensitivity of these two methods could be further investigated so that the optimal one could be used to do the batch processing of all available voxels.

4.5 Conclusion

The three tractography schemes produced false positive (FP) and false negative (FN) white matter pathways in the monkey brain, which might lead to the FP and FN corticocortical connectivity given in chapter III. Comparison of the agreement coefficients for different tractography methods indicates that probabilistic tractography has the potential to provide white matter pathways with better agreement with histology than deterministic tractography does. In addition, the agreement coefficient increases as the d_w of the seed region increases, which is also consistent with the results in Chapter III.

One of the reasons for the disagreement between DTI tractography-derived and histological pathways is that DTI tractography fails to reliably resolve all the orientations of fiber bundle components within one voxel due to the limitation of the tensor model and so on.

CHAPTER V

CONCLUSION AND FUTURE DIRECTIONS

Diffusion tensor imaging (DTI) tractography has the potential to map corticocortical connectivity of human brain non-invasively. However, some well-known factors might corrupt the accuracy and precision of tractography, and hence bias connectivity measurements using DTI. Therefore, whether or to what extent DTI tractography is able to reveal true corticocortical connectivity of the human brain is an important question to be investigated. This dissertation describes the direct comparison of DTI tractography-derived (deterministic and probabilistic tractography) connectivity with the 'ground truth'-neuroanatomical connectivity in the monkey brain—and found that:

(1) DTI tractography is capable of providing true positive connectivity for most or all cortical regions connected anatomically to M1 in the squirrel monkey, but may also produce false positive connections. Deterministic tractography can provide inter-regional connectivity measures as accurate as probabilistic tractography under some situations. DTI tractography is not uniformly sensitive to connection strength either across or within connecting regions.

(2) The three tractography schemes produced false positive and false negative white matter pathways in the monkey brain, which might lead to the false positive and false negative corticocortical connectivity. Probabilistic tractography has the potential to

provide white matter pathways with better agreement with histology than deterministic tractography does. In addition, the agreement coefficient increases as the depth (d_w) of the seed region increases, which is consistent with the corticocortical connectivity results.

(3) A major source of discrepancy between histological and tractography-based connectivity is the presence of crossing fibers, which may prevent streamlines from reaching the correct bundle from the cortical seed region or prevent them from leaving a strongly anisotropic white matter bundle to find the correct cortical terminals. Such failures of DTI tractography might be due to limitations of the single tensor model or the limited sensitivity of the multi-tensor model used in our analysis.

Although only three schemes (i.e., DS, FSL1 and FSL2) were investigated in our study, the correlation procedure proposed here provides a framework for qualitative comparison of more generic tractography-derived connectivity measures with histological connectivity. Therefore, in the future, the entire procedure, especially the neuroanatomical data, are worth distributing in a public resource so more tractography-derived measures of connectivity can be assessed more efficiently.

REFERENCES

1.   Basser, P.J., J. Mattiello, and D. Lebihan, *MR diffusion tensor spectroscopy and imaging.* Biophysical Journal, 1994. **66**(1).

2.   Werring, D.J., et al., *Diffusion tensor imaging can detect and quantify corticospinal tract degeneration after stroke.* Journal of Neurology Neurosurgery and Psychiatry, 2000. **69**(2): p. 269-272.

3.   Horsfield, M.A., et al., *Apparent diffusion coefficients in benign and secondary progressive multiple sclerosis by nuclear magnetic resonance.* Magnetic Resonance in Medicine, 1996. **36**(3): p. 393-400.

4.   Christiansen, P., et al., *Increased water self-diffusion in chronic plaques and in apparently normal white matter in patients with multiple-sclerosis.* Acta Neurologica Scandinavica, 1993. **87**(3): p. 195-199.

5.   Hanyu, H., et al., *Diffusion-weighted MR imaging of the hippocampus and temporal white matter in Alzheimer's disease.* Journal of the Neurological Sciences, 1998. **156**(2): p. 195-200.

6.   Rose, S.E., et al., *Loss of connectivity in Alzheimer's disease: an evaluation of white matter tract integrity with colour coded MR diffusion tensor imaging.* Journal of Neurology Neurosurgery and Psychiatry, 2000. **69**(4): p. 528-530.

7.   Alexopoulos, G.S., et al., *Frontal white matter microstructure and treatment response of late-life depression: A preliminary study.* American Journal of Psychiatry, 2002. **159**(11): p. 1929-1932.

8.   Kubicki, M., et al., *A review of diffusion tensor imaging studies in schizophrenia.* Journal of Psychiatric Research, 2007. **41**(1-2): p. 15-30.

9.   Barnea-Goraly, N., et al., *White matter structure in autism: Preliminary evidence from diffusion tensor imaging.* Biological Psychiatry, 2004. **55**(3): p. 323-326.

10.   Parker, G.J.M., et al., *Lateralization of ventral and dorsal auditory-language pathways in the human brain.* Neuroimage, 2005. **24**(3): p. 656-666.

11.   Oishi, K., et al., *Human brain white matter atlas: Identification and assignment of common anatomical structures in superficial white matter.* Neuroimage, 2008. **43**(3): p. 447-457.

12.   Einstein, A., *On the movement of small particles suspended in stationary liquids required by the molecular-kinetic theroy of heat.* Annalen der physik, 1905. **17**.

13.   Hahn, E.L., *Spin Echoes.* Physical Review, 1950. **80**(4): p. 580-594.

14.   Carr, H. and E. Purcell, *Effects of Diffusion on Free Precession in Nuclear Magnetic Resonance Experiments* Physical review, 1954. **94**(3): p. 630-638.

15.   Torrey, H., *Bloch equations with diffusion terms.* Physical review, 1956. **104**(3): p. 563.

16.   Stejskal, E.O. and J.E. Tanner, *Spin diffusion measurements: Spin echos In The presence of a time-dependent field gradiant.* Journal of Chemical Physics, 1965. **42**(1): p. 288-292.

17.   Basser, P.J., J. Mattiello, and D. Lebihan, *Estimation of the effective self-diffusion tensor from the NMR spin-echo* Journal of Magnetic Resonance Series B, 1994. **103**(3).

18.   Beaulieu, C., *The basis of anisotropic water diffusion in the nervous system - a technical review.* Nmr in Biomedicine, 2002. **15**(7-8): p. 435-455.

19.   Mori, S. and J.Y. Zhang, *Principles of diffusion tensor imaging and its applications to basic neuroscience research.* Neuron, 2006. **51**: p. 527-539.

20.   Basser, P.J., et al., *In vivo fiber tractography using DT-MRI data.* Magnetic Resonance in Medicine, 2000. **44**(4): p. 625-632.

21.   Mori, S., et al., *Three-dimensional tracking of axonal projections in the brain by magnetic resonance imaging.* Annals of Neurology, 1999. **45**(2): p. 265-269.

22. Poupon, C., et al., *Regularization of diffusion-based direction maps for the tracking of brain white matter fascicles.* Neuroimage, 2000. **12**(2): p. 184-195.

23. Westin, C.F., et al., *Processing and visualization for diffusion tensor MRI.* Medical Image Analysis, 2002. **6**(2): p. 93-108.

24. Conturo, T.E., et al., *Tracking neuronal fiber pathways in the living human brain.* Proceedings of the National Academy of Sciences of the United States of America, 1999. **96**(18): p. 10422-10427.

25. Behrens, T.E.J., et al., *Characterization and propagation of uncertainty in diffusion-weighted MR imaging.* Magnetic Resonance in Medicine, 2003. **50**(5): p. 1077-1088.

26. Behrens, T.E.J., et al., *Probabilistic diffusion tractography with multiple fibre orientations: What can we gain?* Neuroimage, 2007. **34**(1): p. 144-155.

27. Mori, S. and P.C.M. van Zijl, *Fiber tracking: principles and strategies - a technical review.* Nmr in Biomedicine, 2002. **15**(7-8): p. 468-480.

28. Singer, C., *Vesalius on the human brain*. 1952, Oxford: Oxford University Press.

29. Marchi, V. and G. Algeri, *Sulle degenerazioni discendenti consecutive a lesioni sperimentali in diverse zone della corteccia cerebrale.* Riv Sper Freniatria Med Legal, 1885. **11**: p. 492-494.

30. Waller, A., *Experiments on the section of the glossopharyngeal and hypoglossal nerves of the frog and observations of the alterations produced thereby in the structures of their primitive fibers.* Phil. Trans. R. Soc. A 1850. **140**: p. 423-429.

31. Nauta, W.J.H., *Some early travails of tracing axonal pathways in the brain.* Journal of Neuroscience, 1993. **13**(4): p. 1337-1345.

32. Morecraft, R.J., et al., *Classic and contemporary neural tract tracing techniques*, in *Diffusion MRI: from quantitative measurement to in-vivo neuroanatomy*. 2009, Adademic press. p. 274-307.

33. Kristens, K. and Y. Olsson, *Retrograde axonal transport of protein.* Brain Research, 1971. **29**(2): p. 363-365.

34. La Vail, J.H. and M.M. La Vail, *Retrograde axonal transport in central nervous-system.* Science, 1972. **176**(4042): p. 1416-1417.

35. Schwab, M.E., F. Javoyagid, and Y. Agid, *Labled wheat-germ agglutinin (WGA) as a new, highly sensitive retrograde tracer in rat-brain hippocampal system.* Brain Research, 1978. **152**(1): p. 145-150.

36. Stoeckel, K., M. Schwab, and H. Thoenen, *Role of gangliosides in uptake and retrograde axonal-transport of cholera and tetanus toxin as compared to nerve growth-factor and wheat-germ agglutinin.* Brain Research, 1977. **132**(2): p. 273-285.

37. Trojanowski, J.Q., J.O. Gonatas, and N.K. Gonatas, *Conjugates of horseradish-peroxidase (HRP) with cholera-toxin and wheat-germ-agglutinin are superior to free HRP as orthogradely transported markers.* Brain Research, 1981. **223**(2): p. 381-385.

38. Kuypers, H., C.E. Catsmanberrevoets, and R.E. Padt, *Retrograde axonal transport of fluorescent substances in rats forebrain.* Neuroscience Letters, 1977. **6**(2-3): p. 127-135.

39. Bentivoglio, M., et al., *Fluorescent retrograde neuronal labeling in rat by means of substances binding specifically to adenine-thymine rich DNA.* Neuroscience Letters, 1979. **12**(2-3): p. 235-240.

40. Ugolini, G., H. Kuypers, and A. Simmons, *Retrograde trans-neuronal transfer of herpes-simplex virus type-1 (HSV 1) from motoneurons.* Brain Research, 1987. **422**(2): p. 242-256.

41. Xue, R., et al., *In vivo three-dimensional reconstruction of rat brain axonal projections by diffusion tensor imaging.* Magnetic Resonance in Medicine, 1999. **42**(6): p. 1123-1127.

42. Catani, M., et al., *Virtual in vivo interactive dissection of white matter fasciculi in the human brain.* Neuroimage, 2002. **17**(1): p. 77-94.

43.   Hagmann, P., et al., *DTI mapping of human brain connectivity: statistical fibre tracking and virtual dissection.* Neuroimage, 2003. **19**(3): p. 545-554.

44.   Behrens, T.E.J., et al., *Non-invasive mapping of connections between human thalamus and cortex using diffusion imaging.* Nature Neuroscience, 2003. **6**(7): p. 750-757.

45.   Johansen-Berg, H., et al., *Changes in connectivity profiles define functionally distinct regions in human medial frontal cortex.* Proceedings of the National Academy of Sciences of the United States of America, 2004. **101**(36): p. 13335-13340.

46.   Anderson, A.W., *Theoretical analysis of the effects of noise on diffusion tensor imaging.* Magnetic Resonance in Medicine, 2001. **46**(6): p. 1174-1188.

47.   Alexander, A.L., et al., *Analysis of partial volume effects in diffusion-tensor MRI.* Magnetic Resonance in Medicine, 2001. **45**(5): p. 770-780.

48.   Hubbard, P.L. and G.J.M. Parker, *Validation of tractography*, in *Diffusion MRI: from quantitative measurement to in-vivo neuroanatomy*, H. Johansen-Berg and T.E.J. Behrens, Editors. 2009, Academic press. p. 353-376.

49.   Lawes, I.N.C., et al., *Atlas-based segmentation of white matter tracts of the human brain using diffusion tensor tractography and comparison with classical dissection.* Neuroimage, 2008. **39**(1): p. 62-79.

50.   Dyrby, T.B., et al., *Validation of in vitro probabilistic tractography.* Neuroimage, 2007. **37**(4): p. 1267-1277.

51.   Dauguet, J., et al., *Comparison of fiber tracts derived from in-vivo DTI tractography with 3D histological neural tract tracer reconstruction on a macaque brain.* Neuroimage, 2007. **37**(2): p. 530-538.

52.   Burgel, U., et al., *White matter fiber tracts of the human brain: Three-dimensional mapping at microscopic resolution, topography and intersubject variability.* Neuroimage, 2006. **29**(4): p. 1092-1105.

53.   Dice, L., *Measures of the amount of ecologic association between species.*

Ecology, 1945. **26**.

54.   Parker, G.J.M., H.A. Haroon, and C.A.M. Wheeler-Kingshott, *A framework for a streamline-based probabilistic index of connectivity (PICo) using a structural interpretation of MRI diffusion measurements.* Journal of Magnetic Resonance Imaging, 2003. **18**(2): p. 242-254.

55.   Flint, J.J., et al., *Cellular-level diffusion tensor microscopy and fiber tracking in mammalian nervous tissue with direct histological correlation.* Neuroimage, 2010. **52**(2): p. 556-561.

56.   Massin, C., et al., *High-Q factor RF planar microcoils for micro-scale NMR spectroscopy.* Sensors and Actuators a-Physical, 2002. **97-8**: p. 280-288.

57.   Weiger, M., et al., *NMR Microscopy with isotropic resolution of 3.0 mu m using dedicated hardware and optimized methods.* Concepts in Magnetic Resonance Part B-Magnetic Resonance Engineering, 2008. **33B**(2): p. 84-93.

58.   Johansen-Berg, H., et al., *Functional-anatomical validation and individual variation of diffusion tractography-based segmentation of the human thalamus.* Cerebral Cortex, 2005. **15**(1): p. 31-39.

59.   Klein, J.C., et al., *Connectivity-based parcellation of human cortex using diffusion MRI: Establishing reproducibility, validity and observer independence in BA 44/45 and SMA/pre-SMA.* Neuroimage, 2007. **34**(1): p. 204-211.

60.   Stephan, K.E., et al., *Advanced database methodology for the Collation of Connectivity data on the Macaque brain (CoCoMac).* Philosophical Transactions of the Royal Society of London Series B-Biological Sciences, 2001. **356**(1412): p. 1159-1186.

61.   Hagmann, P., et al., *Mapping the structural core of human cerebral cortex.* Plos Biology, 2008. **6**(7): p. 1479-1493.

62.   Reiner, A., et al., *Pathway tracing using biotinylated dextran amines.* Journal of Neuroscience Methods, 2000. **103**(1): p. 23-37.

63.   Jones, D.K. and M. Cercignani, *Twenty-five Pitfalls in the Analysis of Diffusion*

MRI Data. Nmr in Biomedicine, 2010. **23**(7): p. 803-820.

64.   Lazar, M. and A.L. Alexander, *Bootstrap white matter tractography (BOOT-TRAC).* Neuroimage, 2005. **24**(2): p. 524-532.

65.   Friman, O., G. Farneback, and C.F. Westin, *A Bayesian approach for stochastic white matter tractography.* Ieee Transactions on Medical Imaging, 2006. **25**(8): p. 965-978.

66.   Hagmann, P., et al., *Mapping Human Whole-Brain Structural Networks with Diffusion MRI.* Plos One, 2007. **2**(7): p. 9.

67.   Vercelli, A., et al., *Recent techniques for tracing pathways in the central nervous system of developing and adult mammals.* Brain Research Bulletin, 2000. **51**(1).

68.   Pautler, R.G., A.C. Silva, and A.P. Koretsky, *In vivo neuronal tract tracing using manganese-enhanced magnetic resonance imaging.* Magnetic Resonance in Medicine, 1998. **40**(5): p. 740-748.

69.   Hofer, S. and J. Frahm, *Topography of the human corpus callosum revisited - Comprehensive fiber tractography using diffusion tensor magnetic resonance imaging.* Neuroimage, 2006. **32**(3): p. 989-994.

70.   Stepniewska, I., T.M. Preuss, and J.H. Kaas, *Architectonics, somatotopic orgnizations, and ipsilateral cortical connections of the primary motor area (M1) of owl monkeys.* Journal of Comparative Neurology, 1993. **330**(2): p. 238-271.

71.   D'Arceuil, H.E., S. Westmoreland, and A.J. de Crespigny, *An approach to high resolution diffusion tensor imaging in fixed primate brain.* NeuroImage, 2007. **35**(2): p. 553-565.

72.   Bookstein, F.L., *Principal warps - thin-plate splines and the decomposition of deformations.* Ieee Transactions on Pattern Analysis and Machine Intelligence, 1989. **11**(6): p. 567-585.

73.   Rohde, G.K., A. Aldroubi, and B.M. Dawant, *The adaptive bases algorithm for intensity-based nonrigid image registration.* Ieee Transactions on Medical

Imaging, 2003. **22**(11): p. 1470-1479.

74. Choe, A., et al., *Accuracy of image registration between MRI and light microscopy in the ex vivo brain.* Magnetic Resonance Imaging, 2011. **29**(5): p. 683-692.

75. Li, C., et al., *A variational level set approach to segmentation and bias correction of images with intensity inhomogeneity*, in *MICCAI*2008. p. 1083-1091.

76. Jiang, H.Y., et al., *DtiStudio: Resource program for diffusion tensor computation and fiber bundle tracking.* Computer Methods and Programs in Biomedicine, 2006. **81**(2): p. 106-116.

77. Chung, S., Y. Lu, and R.G. Henry, *Comparison of bootstrap approaches for estimation of uncertainties of DTI parameters.* Neuroimage, 2006. **33**(2): p. 531-541.

78. Preuss, T.M., I. Stepniewska, and J.H. Kaas, *Movement representation in the dorsal and ventral premotor areas of owl monkeys: A microstimulation study.* Journal of Comparative Neurology, 1996. **371**(4): p. 649-675.

79. Kobbert, C., et al., *Current concepts in neuroanatomical tracing.* Progress in Neurobiology, 2000. **62**(4): p. 327-351.

80. Alexander, D.C., et al., *Spatial transformations of diffusion tensor magnetic resonance images.* IEEE Transactions on Medical Imaging, 2001. **20**(11): p. 1131-1139.

81. McNally, J.G., et al., *Three-dimensional imaging by deconvolution microscopy.* Methods-a Companion to Methods in Enzymology, 1999. **19**(3): p. 373-385.

82. Choe, A.S., et al., *Validation of diffusion tensor MRI in the central nervous system using light microscopy: quantitative comparison of fiber properties.* Nmr in Biomedicine, 2012. **25**(7): p. 900-908.

83. Chaudhuri, S., et al., *A Fourier domain directional filtering method for analysis of collagen alignment in ligaments.* Ieee Transactions on Biomedical Engineering,

1987. **34**(7): p. 509-518.

84.   Anderson, A.W., *Measurement of fiber orientation distributions using high angular resolution diffusion imaging.* Magnetic Resonance in Medicine, 2005. **54**(5): p. 1194-1206.

85.   Lee, T.C., R.L. Kashyap, and C.N. Chu, *Building skeleton models via 3-D medial surface aixs thinning algorithms* Cvgip-Graphical Models and Image Processing, 1994. **56**(6).